



# CHORUS

This is the accepted manuscript made available via CHORUS. The article has been published as:

## Superconductivity by hidden spin fluctuations in electron-doped iron selenide

J. P. Rodriguez

Phys. Rev. B **103**, 184513 — Published 21 May 2021

DOI: [10.1103/PhysRevB.103.184513](https://doi.org/10.1103/PhysRevB.103.184513)

# Superconductivity by Hidden Spin Fluctuations in Electron-Doped Iron Selenide

J.P. Rodriguez<sup>1</sup>

<sup>1</sup>*Department of Physics and Astronomy,  
California State University, Los Angeles, California 90032*

## Abstract

Berg, Metlitski and Sachdev, *Science* **338**, 1606 (2012), have shown that the exchange of hidden spin fluctuations by conduction electrons with two orbitals can result in high-temperature superconductivity in copper-oxide materials. We introduce a similar model for high-temperature iron-selenide superconductors that are electron doped. Conduction electrons carry the minimal  $3d_{xz}$  and  $3d_{yz}$  iron-atom orbitals. Low-energy hidden spin fluctuations at the checkerboard wavevector  $\mathbf{Q}_{AF}$  result from nested Fermi surfaces at the center and at the corner of the unfolded (one-iron) Brillouin zone. Magnetic frustration from super-exchange interactions via the selenium atoms stabilize hidden spin fluctuations at  $\mathbf{Q}_{AF}$  versus true spin fluctuations. At half filling, Eliashberg theory based purely on the exchange of hidden spin fluctuations reveals a Lifshitz transition to electron/hole Fermi surface pockets at the corner of the folded (two-iron) Brillouin zone, but with vanishing spectral weights. The underlying hidden spin-density wave groundstate is therefore a Mott insulator. Upon electron doping, Eliashberg theory finds that the spectral weights of the hole Fermi surface pockets remain vanishingly small, while the spectral weights of the larger electron Fermi surface pockets become appreciable. This prediction is therefore consistent with the observation of electron Fermi surface pockets alone in electron-doped iron selenide by angle-resolved photoemission spectroscopy (ARPES). Eliashberg theory also finds an instability to  $S^{+-}$  superconductivity at electron doping, with isotropic Cooper pairs that alternate in sign between the visible electron Fermi surface pockets and the faint hole Fermi surface pockets. Comparison with the isotropic energy gaps observed in electron-doped iron selenide by ARPES and by scanning tunneling microscopy (STM) is consistent with short-range hidden magnetic order.

## I. INTRODUCTION

Electron-doped iron selenides are perhaps the most interesting class of materials inside the family of iron-based superconductors<sup>1-4</sup>. By contrast with bulk FeSe, which is a low-temperature superconductor, a monolayer of FeSe on a doped strontium-titanate substrate becomes a high-temperature superconductor<sup>5</sup>, with a critical temperature in the range 40-50 K<sup>6,7</sup>, and possibly higher<sup>8</sup>. Angle-resolved photoemission spectroscopy (ARPES) reveals that the substrate injects electrons into the FeSe monolayer that bury the hole bands at the center of the Brillouin zone below the Fermi level<sup>9</sup>. ARPES also reveals an energy gap at the remaining electron-type Fermi surface pockets at the corner of the folded (two-iron) Brillouin zone<sup>10,11</sup>. It agrees with the energy gap found by scanning tunneling microscopy (STM)<sup>5,12</sup>. On the other hand, transport studies find perfect conductivity below the critical temperature where the gap opens in ARPES and in STM<sup>6,8</sup>. These probes provide compelling evidence for a superconducting state at high temperature. Electron doping of FeSe layers can also be achieved by other means, such as by alkali-atom intercalation<sup>1-4</sup>, and by organic-molecule intercalation<sup>13-15</sup>. These systems show the same Lifshitz transition of the Fermi surface topology, where the hole bands are buried below the Fermi level at the  $\Gamma$ -point, but where electron Fermi surface pockets at the corner of the folded Brillouin zone remain. These systems also show high-temperature superconductivity, with an isotropic energy gap that opens at the electron-type Fermi surface pockets.

The coincidence of high-temperature superconductivity with the absence of Fermi surface nesting in electron-doped FeSe is puzzling. High-temperature superconductivity in iron-pnictide materials occurs only when the Fermi surfaces exhibit partial nesting, for example. In particular, the end-member compound  $\text{KFe}_2\text{As}_2$  of the series of iron-pnictide compounds<sup>16</sup>  $(\text{Ba}_{1-x}\text{K}_x)\text{Fe}_2\text{As}_2$  shows hole-type Fermi surface pockets at the center of the Brillouin zone, but no electron Fermi surface pockets at the corner of the folded Brillouin zone to nest with<sup>17</sup>. It is a low-temperature superconductor with  $T_c \cong 3$  K, however. Early theoretical responses to the puzzle posed by electron-doped iron selenide proposed a nodeless  $D$ -wave superconducting state<sup>18,19</sup>, with a full gap over each electron pocket that alternates in sign between them. In the case of bulk electron-doped iron-selenide materials, it was argued that strong dispersion of the energy bands along the  $c$  axis results in inner and outer electron Fermi surface pockets at the corner of the folded Brillouin zone because of hybridization due

to the two inequivalent iron sites, and that true  $D$ -wave nodes appear as a result<sup>20</sup>. In the case of an isolated layer of FeSe, the two electron Fermi surface pockets at the corner of the two-iron Brillouin zone cross, but do not hybridize, because of glide-reflection symmetry<sup>21</sup>. Inner and outer electron Fermi surface pockets due to hybridization are predicted when strong enough spin-orbit coupling is included, however, and true  $D$ -wave nodes are again predicted<sup>22,23</sup>. These considerations led to the proposal of the anti-bonding  $S^{+-}$  state. It is an isotropic Cooper pair state that alternates in sign between the inner and the outer electron Fermi surfaces at the corner of the folded (two-iron) Brillouin zone<sup>20,24</sup>. ARPES finds no sign of nodes in the gap and no sign of hybridization on the electron Fermi surface pockets<sup>10,11</sup>, however. Further, STM and the dependence of the specific heat and of nuclear magnetic resonance (NMR) on temperature are consistent with a gap over the entire Fermi surface<sup>3-5</sup>. These measurements could then rule out the nodeless  $D$ -wave state and the anti-bonding  $S^{+-}$  state in high- $T_c$  iron-selenide superconductors.

Below, we will show that a spin-fermion model over the square lattice that is similar to that introduced by Berg, Metlitski and Sachdev in the context of copper-oxide high-temperature superconductors<sup>25</sup> harbors an alternative solution to the puzzling isotropic gap shown by electron-doped iron selenide. The non-interacting electrons are in the principal  $3d_{xz}$  and  $3d_{yz}$  iron orbitals, and they form a semi-metallic Fermi surface that is nested by the checkerboard wavevector  $\mathbf{Q}_{AF} = (\pi/a, \pi/a)$ . The latter can result in hidden magnetic order when magnetic frustration is present, at weak enough Hund's Rule coupling<sup>26</sup>. Such hidden antiferromagnetism is characterized by the most symmetric of three possible order parameters for a hidden spin density wave (hSDW):

$$\frac{1}{2\mathcal{N}} \sum_i e^{i\mathbf{Q}_{AF}\cdot\mathbf{r}_i} \sum_{s=\uparrow,\downarrow} (\text{sgn } s) i \langle c_{i,dxz,s}^\dagger c_{i,dyz,s} - c_{i,dyz,s}^\dagger c_{i,dxz,s} \rangle,$$

where  $\mathcal{N}$  is the number of site-orbitals. It is isotropic with respect to rotations of the orbitals about the  $z$  axis, and it therefore does not couple to nematicity. (Cf. refs.<sup>27,28</sup>.) Based on the interaction of such fermions with the corresponding hidden spin fluctuations, an Eliashberg theory for  $S$ -wave pairing over the two bands of electrons is developed. Hopping matrix elements are chosen so that perfect nesting exists at half filling<sup>26</sup>. As the interaction grows strong, we find (i) a Lifshitz transition to electron-type and hole-type Fermi surface pockets at the corner of the folded (two-iron) Brillouin zone. The new Fermi surfaces remain perfectly nested by  $\mathbf{Q}_{AF}$ , but their spectral weights are vanishingly small due to strong wave-

function renormalization. Upon electron doping, the hole Fermi surfaces remain faint, while the electron Fermi surfaces become visible because of only moderate wavefunction renormalization. This prediction agrees with previous calculations based on the corresponding local-moment model<sup>29</sup>. The Eliashberg theory also reveals (*ii*) an instability at the renormalized Fermi surface to  $S^{+-}$  pairing that alternates in sign between the visible electron-type Fermi surfaces and the faint hole-type Fermi surfaces. We shall now provide details of how such hidden  $S^{+-}$  superconductivity emerges from the two-band Eliashberg theory.

## II. BARE NESTED FERMI SURFACES AND HIDDEN SPIN FLUCTUATIONS

The conditions for perfect nesting of the Fermi surfaces in two-orbital hopping Hamiltonians for iron selenide will be determined in what follows<sup>26</sup>. Also, the space of hSWD states generated by rotations of the two isospin degrees of freedom, the  $d+$  and  $d-$  orbitals, will be discussed.

### A. Electron Hopping

The electronic kinetic energy is governed by the hopping Hamiltonian

$$H_{\text{hop}} = - \sum_{\langle i,j \rangle} (t_1^{\alpha,\beta} c_{i,\alpha,s}^\dagger c_{j,\beta,s} + \text{h.c.}) - \sum_{\langle\langle i,j \rangle\rangle} (t_2^{\alpha,\beta} c_{i,\alpha,s}^\dagger c_{j,\beta,s} + \text{h.c.}), \quad (1)$$

where the repeated indices  $\alpha$  and  $\beta$  are summed over the iron  $d+$  and  $d-$  orbitals, where the repeated index  $s$  is summed over electron spin, and where  $\langle i,j \rangle$  and  $\langle\langle i,j \rangle\rangle$  represent nearest neighbor (1) and next-nearest neighbor (2) links on the square lattice of iron atoms. Above,  $c_{i,\alpha,s}$  and  $c_{i,\alpha,s}^\dagger$  denote annihilation and creation operators for an electron of spin  $s$  in orbital  $\alpha$  at site  $i$ . We keep only the  $3d_{xz}$  and  $3d_{yz}$  orbitals of the iron atoms, which are the principal ones in iron selenide. In particular, let us work in the isotropic basis of orbitals  $d- = (d_{xz} - id_{yz})/\sqrt{2}$  and  $d+ = (d_{xz} + id_{yz})/\sqrt{2}$ . The reflection symmetries shown by a single layer of iron selenide imply that the above intra-orbital and inter-orbital hopping matrix elements show  $s$ -wave and  $d$ -wave symmetry, respectively<sup>21,30,31</sup>. In particular, nearest neighbor hopping matrix elements satisfy

$$\begin{aligned} t_1^{\pm\pm}(\hat{\mathbf{x}}) &= t_1^\parallel = t_1^{\pm\pm}(\hat{\mathbf{y}}) \\ t_1^{\pm\mp}(\hat{\mathbf{x}}) &= t_1^\perp = -t_1^{\pm\mp}(\hat{\mathbf{y}}), \end{aligned} \quad (2)$$

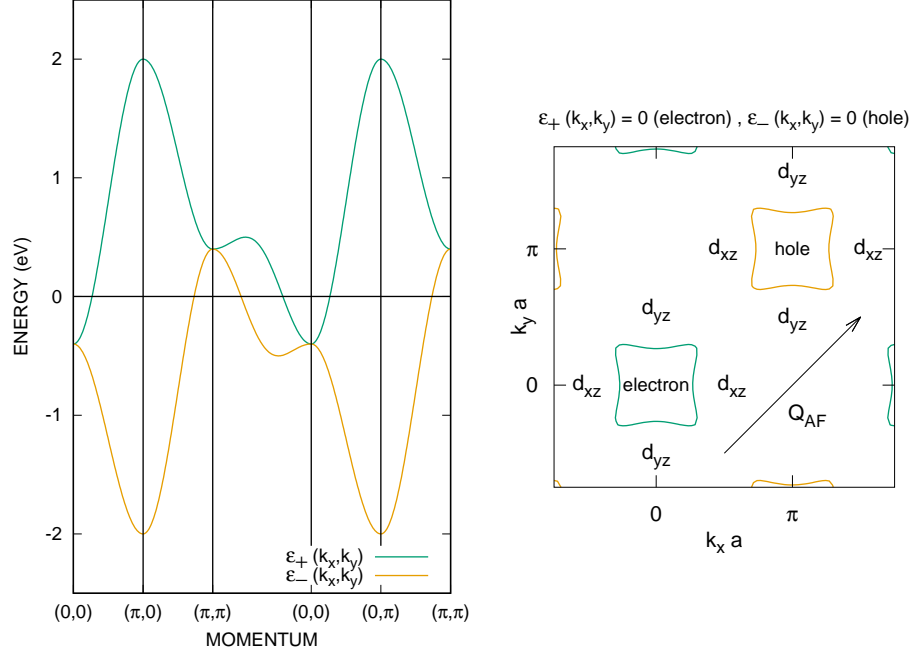


FIG. 1: Band structure with perfectly nested Fermi surfaces at half filling:  $\varepsilon_+(\mathbf{k}) = 0$  and  $\varepsilon_-(\mathbf{k}) = 0$ , with hopping matrix elements  $t_1^{\parallel} = 100$  meV,  $t_1^{\perp} = 500$  meV,  $t_2^{\parallel} = 0$ , and  $t_2^{\perp}/i = 100$  meV.

where  $t_1^{\parallel}$  and  $t_1^{\perp}$  are real, while next-nearest neighbor hopping matrix elements satisfy

$$\begin{aligned} t_2^{\pm\pm}(\hat{\mathbf{x}} + \hat{\mathbf{y}}) &= t_2^{\parallel} = t_2^{\pm\pm}(\hat{\mathbf{y}} - \hat{\mathbf{x}}) \\ t_2^{\pm\mp}(\hat{\mathbf{x}} + \hat{\mathbf{y}}) &= \pm t_2^{\perp} = -t_2^{\pm\mp}(\hat{\mathbf{y}} - \hat{\mathbf{x}}), \end{aligned} \quad (3)$$

where  $t_2^{\parallel}$  is real, and where  $t_2^{\perp}$  is pure imaginary.

The above hopping Hamiltonian  $H_{\text{hop}}$  then has intra-orbital and inter-orbital matrix elements

$$\varepsilon_{\parallel}(\mathbf{k}) = -2t_1^{\parallel}(\cos k_x a + \cos k_y a) - 2t_2^{\parallel}(\cos k_+ a + \cos k_- a) \quad (4a)$$

$$\varepsilon_{\perp}(\mathbf{k}) = -2t_1^{\perp}(\cos k_x a - \cos k_y a) - 2t_2^{\perp}(\cos k_+ a - \cos k_- a) \quad (4b)$$

with  $k_{\pm} = k_x \pm k_y$ . It is easily diagonalized by plane waves of  $d_{x(\delta)z}$  and  $id_{y(\delta)z}$  orbitals that are rotated with respect to the principal axes by an angle  $\delta(\mathbf{k})$ :

$$\begin{aligned} |\mathbf{k}, d_{x(\delta)z}\rangle &= \mathcal{N}^{-1/2} \sum_i e^{i\mathbf{k}\cdot\mathbf{r}_i} [e^{i\delta(\mathbf{k})} |i, d+\rangle + e^{-i\delta(\mathbf{k})} |i, d-\rangle], \\ i|\mathbf{k}, d_{y(\delta)z}\rangle &= \mathcal{N}^{-1/2} \sum_i e^{i\mathbf{k}\cdot\mathbf{r}_i} [e^{i\delta(\mathbf{k})} |i, d+\rangle - e^{-i\delta(\mathbf{k})} |i, d-\rangle], \end{aligned} \quad (5)$$

where  $\mathcal{N} = 2N_{\text{Fe}}$  is the number of iron site-orbitals. The phase shift  $\delta(\mathbf{k})$  is set by  $\varepsilon_{\perp}(\mathbf{k}) = |\varepsilon_{\perp}(\mathbf{k})|e^{i2\delta(\mathbf{k})}$ . Specifically,

$$\cos 2\delta(\mathbf{k}) = \frac{-t_1^{\perp}(\cos k_x a - \cos k_y a)}{\sqrt{t_1^{\perp 2}(\cos k_x a - \cos k_y a)^2 + |2t_2^{\perp}|^2(\sin k_x a)^2(\sin k_y a)^2}}, \quad (6a)$$

$$\sin 2\delta(\mathbf{k}) = \frac{2(t_2^{\perp}/i)(\sin k_x a)(\sin k_y a)}{\sqrt{t_1^{\perp 2}(\cos k_x a - \cos k_y a)^2 + |2t_2^{\perp}|^2(\sin k_x a)^2(\sin k_y a)^2}}. \quad (6b)$$

The phase shift is notably singular at  $\mathbf{k} = 0$  and  $\mathbf{Q}_{\text{AF}} = (\pi/a, \pi/a)$ , where the matrix element  $\varepsilon_{\perp}(\mathbf{k})$  vanishes. The energy eigenvalues of the bonding (+) and anti-bonding (-) plane waves (5) are respectively given by  $\varepsilon_+(\mathbf{k}) = \varepsilon_{\parallel}(\mathbf{k}) + |\varepsilon_{\perp}(\mathbf{k})|$  and  $\varepsilon_-(\mathbf{k}) = \varepsilon_{\parallel}(\mathbf{k}) - |\varepsilon_{\perp}(\mathbf{k})|$ .

Henceforth, we shall turn off next-nearest neighbor intra-orbital hopping:  $t_2^{\parallel} = 0$ . Notice that the above energy bands now satisfy the perfect nesting condition

$$\varepsilon_{\pm}(\mathbf{k} + \mathbf{Q}_{\text{AF}}) = -\varepsilon_{\mp}(\mathbf{k}), \quad (7)$$

where  $\mathbf{Q}_{\text{AF}} = (\pi/a, \pi/a)$  is the wavevector for the checkerboard on the square lattice of iron atoms. The Fermi level at half filling therefore lies at  $\epsilon_{\text{F}} = 0$ . Figure 1 displays perfectly nested electron-type and hole-type Fermi surfaces for hopping parameters  $t_1^{\parallel} = 100$  meV,  $t_1^{\perp} = 500$  meV,  $t_2^{\parallel} = 0$  and  $t_2^{\perp}/i = 100$  meV. Figure 2 shows the density of states of the bonding (+) band.

## B. Extended Hubbard Model

The Hamiltonian of the underlying extended Hubbard model<sup>26</sup> has three parts:  $H = H_{\text{hop}} + H_U + H_{\text{sprx}}$ . On-site Coulomb repulsion is counted by the second term<sup>32</sup>,

$$H_U = \sum_i [U_0 n_{i,\alpha,\uparrow} n_{i,\alpha,\downarrow} + J_0 \mathbf{S}_{i,d-} \cdot \mathbf{S}_{i,d+} + U'_0 n_{i,d+} n_{i,d-} + J'_0 (c_{i,d+,\uparrow}^{\dagger} c_{i,d+,\downarrow}^{\dagger} c_{i,d-,\downarrow} c_{i,d-,\uparrow} + \text{h.c.})]. \quad (8)$$

where  $n_{i,\alpha,s}$  is the occupation operator, and where  $n_{i,\alpha} = n_{i,\alpha,\uparrow} + n_{i,\alpha,\downarrow}$ . Also,  $\mathbf{S}_{i,\alpha}$  is the spin operator. Above,  $U_0 > 0$  is the intra-orbital on-site Coulomb repulsion energy, while  $U'_0 > 0$  is the inter-orbital one. It is worth pointing out the following expression for the sum of these two on-site repulsion terms in (8):

$$U_0 n_{i,\alpha,\uparrow} n_{i,\alpha,\downarrow} + U'_0 n_{i,d+} n_{i,d-} = (U_0 - U'_0) n_{i,\alpha,\uparrow} n_{i,\alpha,\downarrow} + \frac{1}{2} U'_0 n_i (n_i - 1), \quad (9)$$

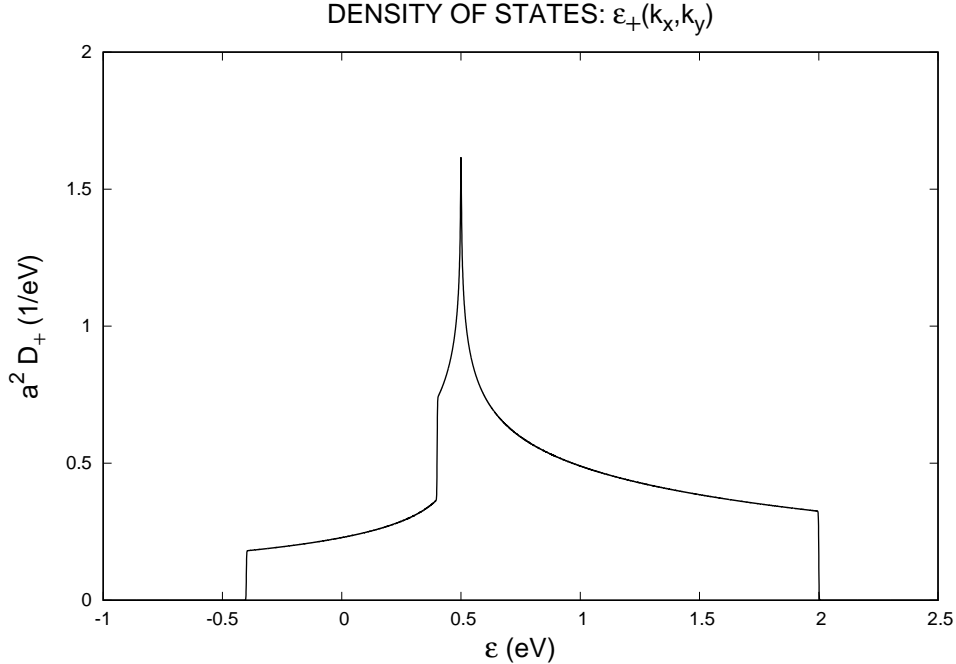


FIG. 2: Density of states of the bonding band evaluated numerically at hopping parameters that are listed in the caption to Fig. 1:  $a^2 D_+(\varepsilon) = N_{\text{Fe}}^{-1} \sum_{\mathbf{k}} \delta[\varepsilon - \varepsilon_+(\mathbf{k})]$ . The unfolded (one-iron) Brillouin zone is divided into a  $10,000 \times 10,000$  grid, while the  $\delta$ -function is approximated by  $(4k_B T_0)^{-1} \text{sech}^2(\varepsilon/2k_B T_0)$ . Here,  $k_B T_0$  is 3 parts in 10,000 of the bandwidth.

where  $n_i = n_{i,d+} + n_{i,d-}$  is the net occupation per iron site  $i$ . Above also,  $J_0$  is the Hund's Rule exchange coupling constant, which has a ferromagnetic (negative) sign, while  $J'_0$  is the matrix element for on-site Josephson tunneling between orbitals. The third and last term in the Hamiltonian represents super-exchange interactions among the iron spins via the selenium atoms:

$$\begin{aligned}
 H_{\text{sprx}} = & \sum_{\langle i,j \rangle} J_1^{(\text{sprx})} (\mathbf{S}_{i,d-} + \mathbf{S}_{i,d+}) \cdot (\mathbf{S}_{j,d-} + \mathbf{S}_{j,d+}) \\
 & + \sum_{\langle\langle i,j \rangle\rangle} J_2^{(\text{sprx})} (\mathbf{S}_{i,d-} + \mathbf{S}_{i,d+}) \cdot (\mathbf{S}_{j,d-} + \mathbf{S}_{j,d+}). \quad (10)
 \end{aligned}$$

Above,  $J_1^{(\text{sprx})}$  and  $J_2^{(\text{sprx})}$  are positive super-exchange coupling constants over nearest neighbor and next-nearest neighbor iron sites.

It is instructive to uncover the energy spectrum of the Hamiltonian  $H_U$  at a single iron site  $i$ , at half filling with two electrons. Table I gives the corresponding six-dimensional Hilbert space in the singlet-triplet/spin-isospin basis. Here, the  $d+$  and the  $d-$  orbitals comprise the



| $I^{(3)} \mid S^{(z)}/\hbar$ | isospin triplet ( $I = 1$ ), spin singlet ( $S = 0$ )  | isospin singlet ( $I = 0$ ), spin triplet ( $S = 1$ )  |
|------------------------------|--|--|
| +1                           | $d_{+1}d_{+2}\frac{1}{\sqrt{2}}(\uparrow_1\downarrow_2 - \downarrow_1\uparrow_2)$                                    | $\frac{1}{\sqrt{2}}(d_{+1}d_{-2} - d_{-1}d_{+2})\uparrow_1\uparrow_2$  |
| 0                            | $\frac{1}{\sqrt{2}}(d_{+1}d_{-2} + d_{-1}d_{+2})\frac{1}{\sqrt{2}}(\uparrow_1\downarrow_2 - \downarrow_1\uparrow_2)$ | $\frac{1}{\sqrt{2}}(d_{+1}d_{-2} - d_{-1}d_{+2})\frac{1}{\sqrt{2}}(\uparrow_1\downarrow_2 + \downarrow_1\uparrow_2)$ |
| -1                           | $d_{-1}d_{-2}\frac{1}{\sqrt{2}}(\uparrow_1\downarrow_2 - \downarrow_1\uparrow_2)$                                    | $\frac{1}{\sqrt{2}}(d_{+1}d_{-2} - d_{-1}d_{+2})\downarrow_1\downarrow_2$  |

TABLE I: Atomic iron states at half filling. The isospin triplet states violate Hund's Rule, while the isospin singlet states obey Hund's Rule.

isospin-1/2 states. Specifically, the isospin operators along the axes  $n = 1, 2, 3$  for a single electron have the form  $I^{(n)} = +\frac{1}{2}|u_n\rangle\langle u_n| - \frac{1}{2}|v_n\rangle\langle v_n|$ , with orbitals  $(u_1, v_1) = (d_{xz}, d_{yz})$ ,  $(u_2, v_2) = (d_{x'z}, d_{y'z})$ , and  $(u_3, v_3) = (d_+, d_-)$ . Here,  $x' = (x + y)/\sqrt{2}$  and  $y' = (-x + y)/\sqrt{2}$ . The eigenstates of (8) at a single iron site are the product of spin ( $S = 1$ ) triplet states with the isospin ( $I = 0$ ) singlet state

$$\phi_0(1, 2) = \frac{1}{\sqrt{2}}[u_n(1)v_n(2) - v_n(1)u_n(2)], \quad (11)$$

and the product of the spin ( $S = 0$ ) singlet state with the isospin ( $I = 1$ ) triplet states

$$\phi_n(1, 2) = \frac{1}{\sqrt{2}}[u_n(1)v_n(2) + v_n(1)u_n(2)], \quad n = 1, 2, 3. \quad (12)$$

Recall that the isospin singlet pair state  $\phi_0(1, 2)$  is *unique* up to a phase factor. The orbital pair states (11) and (12) above satisfy  $I^{(n)}\phi_0 = 0$  and  $I^{(n)}\phi_n = 0$ , where  $I^{(n)} = I^{(n)}(1) + I^{(n)}(2)$ . And why do the pair states (11) and (12) make up the energy spectrum of  $H_U$ ? First, observe that the spin singlet and spin triplet states listed in Table I are all eigenstates of the Hund's Rule term in (8), with energy splitting  $E_{\text{singlet}}^{(0)} - E_{\text{triplet}}^{(0)} = -J_0$ . Second, notice that all six pair states listed in Table I are eigenstates of the sum (9) of the intra-orbital and inter-orbital on-site repulsion terms in (8), with energy splitting between the doubly occupied and singly occupied  $d_+$  and  $d_-$  orbitals,  $E_{d(1)d(2)}^{(0)} - E_{d(1)\bar{d}(2)}^{(0)} = U_0 - U'_0$ . Third, notice that the pair states  $\phi_1(1, 2)$  and  $\phi_2(1, 2)$  are odd and even superpositions of  $d_+(1)d_+(2)$  and  $d_-(1)d_-(2)$ . The former pair states, hence, are eigenstates of the on-site Josephson tunneling terms in (8), with energy splitting  $E_1^{(0)} - E_2^{(0)} = -2J'_0$ . The remaining pair states  $\phi_0(1, 2)$  and  $\phi_3(1, 2)$  do not participate in on-site Josephson tunneling. Table II lists the atomic energies of these pair states compared to the one along the isospin  $I^{(3)}$  axis.

Last, we point out that both the on-site Josephson tunneling terms in (8) and the first term in (9) for the on-site repulsion break isospin rotation invariance. Such symmetry-

| Isospin Axis of Pair State ( $n$ ) | $S$ | $I$ | $\Delta H_U$        |
|------------------------------------|-----|-----|---------------------|
| any (0)                            | 1   | 0   | $J_0$               |
| $I^{(1)}$                          | 0   | 1   | $U_0 - U'_0 - J'_0$ |
| $I^{(2)}$                          | 0   | 1   | $U_0 - U'_0 + J'_0$ |
| $I^{(3)}$                          | 0   | 1   | 0                   |

TABLE II: Relative energy  $H_U$  of atomic pair states,  $\phi_n(1, 2)$ , compared to that of  $\phi_3(1, 2)$ . Recall that  $J_0 < 0$ .

breaking contributions in the on-site Hamiltonian  $H_U$  are consolidated by the Hamiltonian

$$H'_U = \sum_i 2[+J'_0 I_{i,\uparrow}^{(1)} I_{i,\downarrow}^{(1)} - J'_0 I_{i,\uparrow}^{(2)} I_{i,\downarrow}^{(2)} + (U_0 - U'_0) I_{i,\uparrow}^{(3)} I_{i,\downarrow}^{(3)}], \quad (13)$$

where  $\mathbf{I}_{i,\uparrow}$  and  $\mathbf{I}_{i,\downarrow}$  are the respective isospin operators for spin- $\uparrow$  and spin- $\downarrow$  electrons at iron site  $i$ . (See Appendix A.) They each represent  $2 \times 2$  isospin operators acting on the  $d+$  and  $d-$  orbitals for an electron of such spin.

### C. Hidden Magnetic Order

The true electronic spin at an iron site  $i$  is measured by the operator  $\mathbf{S}_i = \mathbf{S}_{i,d+} + \mathbf{S}_{i,d-}$ , with  $\mathbf{S}_{i,\alpha} = (\hbar/2) \sum_{s,s'} c_{i,\alpha,s}^\dagger \boldsymbol{\sigma}_{s,s'} c_{i,\alpha,s'}$ , where  $\boldsymbol{\sigma}$  denote the Pauli matrices. In the present case, we keep only the principal  $d-$  and  $d+$  orbitals,  $\alpha$ . Hidden spin excitations must be orthogonal to true spin excitations. Hidden spin excitations then correspond to “pion” excitations of the latter isospin degrees of freedom. Table III lists these spin excitations explicitly, which carry isospin  $I = 1$ . They are isospin components of the tensor product  $(\mathbf{S} \otimes \mathbf{I})_i = (\hbar/4) \sum_{\alpha,\alpha'} \sum_{s,s'} c_{i,\alpha,s}^\dagger \boldsymbol{\sigma}_{s,s'} \boldsymbol{\tau}_{\alpha,\alpha'} c_{i,\alpha',s'}$ , where  $\boldsymbol{\tau}$  also denote the Pauli matrices. (See Appendix A.) Notice that hidden spin excitations generated by the  $(\pi^0)$  operator  $2(\mathbf{S} \otimes I^{(3)})_i = \mathbf{S}_{i,d+} - \mathbf{S}_{i,d-}$  are the most symmetric ones, showing isotropy about the orbital  $z$  axis. This is displayed explicitly by Table IV, in the row corresponding to the isospin quantization axis  $I^{(3)}$ , where  $2(\mathbf{S} \otimes I^{(3)})_i$  is written in terms of  $d_{xz}$  and  $d_{yz}$  orbitals. Figure 3 shows three different hidden spin-density orderings made up, respectively, of the three magnetic moments  $2(\mathbf{S} \otimes I^{(n)})_i$  over the square lattice  $i$ , with  $n = 1, 2, 3$ . Such hSDW groundstates have been introduced recently in the context of copper-oxide high- $T_c$  superconductors<sup>25</sup>, of heavy fermion compounds<sup>33</sup>, and of iron-selenide high- $T_c$  superconductors<sup>26,29</sup>.

| spin operator   | meson analog | $I$ | $I^{(3)}$ | type of spin |
|---|--------------|-----|-----------|--------------|
| $c_{i,d+}^\dagger \boldsymbol{\sigma} c_{i,d+} + c_{i,d-}^\dagger \boldsymbol{\sigma} c_{i,d-}$ | $\omega$     | 0   | 0         | true         |
| $c_{i,d+}^\dagger \boldsymbol{\sigma} c_{i,d+} - c_{i,d-}^\dagger \boldsymbol{\sigma} c_{i,d-}$ | $\pi^0$      | 1   | 0         | hidden       |
| $c_{i,d+}^\dagger \boldsymbol{\sigma} c_{i,d-}$   | $\pi^+$      | 1   | +1        | hidden       |
| $c_{i,d-}^\dagger \boldsymbol{\sigma} c_{i,d+}$   | $\pi^-$      | 1   | -1        | hidden       |

TABLE III: List of spin-excitation operators according to isospin. Above,  $\boldsymbol{\sigma}$  denotes the Pauli matrices for spin, and  $I$  and  $I^{(3)}$  denote the isospin quantum numbers. Summation over spin indices is implicit. Meson analogs are obtained by identifying the  $d+$  orbital with the  $u$  quark and the  $d-$  orbital with the  $d$  quark. See Appendix A for a definition of the isospin operator.

In the last case, perfect nesting of electron-type and hole-type Fermi surfaces exists at half filling and  $t_2^\parallel = 0$ , which is displayed by Fig. 1. This implies an instability to a spin-density wave at the wavevector corresponding to Néel antiferromagnetic order,  $\mathbf{Q}_{\text{AF}} = (\pi/a, \pi/a)$ . The atomic limit discussed at the end of the previous subsection becomes a useful guide to determine the relative stability of the four checkerboard spin density waves displayed by Fig. 3 in the limit of strong on-site repulsion. First, it is important to point out that the on-site pair states that compose the hSDW groundstates displayed by Figs. 3(b)-(d) can be expressed as even and odd superpositions of spin singlet and spin triplet states,

$$\frac{1}{\sqrt{2}}\phi_n(1,2)\frac{1}{\sqrt{2}}(\uparrow_1\downarrow_2 - \downarrow_1\uparrow_2) \pm \frac{1}{\sqrt{2}}\phi_0(1,2)\frac{1}{\sqrt{2}}(\uparrow_1\downarrow_2 + \downarrow_1\uparrow_2), \quad (14)$$

where  $\phi_0(1,2)$  and  $\phi_n(1,2)$  are orbital pair states given by (11) and (12). Such atomic pair states violate Hund's Rule. The corresponding hSDW groundstates therefore compete with the conventional SDW groundstate displayed by Fig. 3(a) in the regime of weak Hund's Rule coupling. Local-moment Heisenberg models find, in particular, that such hSDW states are more stable than both the conventional checkerboard and stripe SDW states in the presence of magnetic frustration (10), at weak enough Hund's Rule coupling<sup>34</sup>. (See Fig. 7.) And which of the three hSDW states displayed by Figs. 3(b)-(d) is the most energetically favorable one? Contrasting the corresponding atomic pair states (14) with the atomic spectrum listed by Table II indicates that the hSDW displayed by Fig. 3(b), which corresponds to the  $I^{(3)}$  isospin axis ( $n = 3$ ), is the lowest in energy at sufficiently large intra-orbital on-site repulsion:  $U_0 - U'_0 > |J'_0|$ . Notice that both the sum of the on-site repulsion terms (9) and the on-site Josephson tunneling terms in the Hamiltonian (8) break

| hidden spin operator   | isospin quantization axis | reference                          |
|--|---------------------------|------------------------------------|
| $c_{i,d_{xz}}^\dagger \boldsymbol{\sigma} c_{i,d_{xz}} - c_{i,d_{yz}}^\dagger \boldsymbol{\sigma} c_{i,d_{yz}}$    | $I^{(1)}$                 | none                               |
| $c_{i,d_{xz}}^\dagger \boldsymbol{\sigma} c_{i,d_{yz}} + c_{i,d_{yz}}^\dagger \boldsymbol{\sigma} c_{i,d_{xz}}$    | $I^{(2)}$                 | Berg, Metlitski and Sachdev (2012) |
| $i(c_{i,d_{xz}}^\dagger \boldsymbol{\sigma} c_{i,d_{yz}} - c_{i,d_{yz}}^\dagger \boldsymbol{\sigma} c_{i,d_{xz}})$ | $I^{(3)}$                 | Rodriguez (2017)                   |

TABLE IV: List of hidden spin-excitation operators by isospin quantization axis. Summation over spin indices is implicit. Examples of where such hidden spin excitations appear in the literature are also listed. Note: the spin operator in the second row ( $I^{(2)}$ ) is diagonal in the orbital basis rotated by 45 degrees about the  $z$  axis;  $c_{i,d_{x'z}}^\dagger \boldsymbol{\sigma} c_{i,d_{x'z}} - c_{i,d_{y'z}}^\dagger \boldsymbol{\sigma} c_{i,d_{y'z}}$ , where  $x' = (x + y)/\sqrt{2}$  and  $y' = (-x + y)/\sqrt{2}$ . See Appendix A for a definition of the isospin operator.

$SU(2)$  isospin rotation invariance. These terms are collected (13) by  $H'_U$ . Last, it is worth re-emphasizing here that the hSDW corresponding to atomic pair states (14) with  $n = 3$  is notably isotropic with respect to rotations of the orbitals about the  $z$  axis.

The long-range hidden Néel order shown by the hSDW state (Fig. 3b) implies low-energy spinwave excitations that collapse to zero energy at the ordering wavevector  $\mathbf{Q}_{\text{AF}}$ . These hidden spinwaves emerge from the dynamics between the bulk spin,  $\mathbf{S} = \sum_i (\mathbf{S}_{i,d-} + \mathbf{S}_{i,d+})$ , and the hidden ordered magnetic moment<sup>26</sup>,  $\mathbf{m}(\pi) = N_{\text{Fe}}^{-1} \sum_i e^{i\mathbf{Q}_{\text{AF}} \cdot \mathbf{r}_i} (\mathbf{S}_{i,d-} - \mathbf{S}_{i,d+})$ . It is yet another example of antiferromagnetic dynamics first discovered by Anderson<sup>35–37</sup>. The dynamical propagator for hidden spinwaves can then be defined as  $iD(\mathbf{q}, \omega) = \langle \frac{1}{\sqrt{2}} m^+(\pi) \frac{1}{\sqrt{2}} m^-(\pi) \rangle_{\mathbf{q}, \omega}$ , where  $m^\pm(\pi) = m_x(\pi) \pm i m_y(\pi)$ . Here, we have assumed that the hSDW spontaneously breaks symmetry along the  $z$  axis. Within the random phase approximation (RPA) of the two-orbital extended Hubbard model, recent calculations of the dynamical spin susceptibility in the hSDW state, Fig. 3b, yield the universal form<sup>36,37</sup>

$$D(\mathbf{q}, \omega) = \frac{(2s_1)^2}{\chi_\perp} [\omega^2 - \omega_b^2(\mathbf{q})]^{-1} \quad (15)$$

at long wavelength and low frequency<sup>38</sup>. Above,  $2s_1\hbar$  is the magnitude of the hidden ordered magnetic moment  $\mathbf{m}(\pi)$  at an iron site, while  $\chi_\perp$  is the spin susceptibility of the hSDW for external magnetic field applied perpendicular to  $\mathbf{m}(\pi)$ . The poles in frequency in (15) disperse as

$$\omega_b(\mathbf{q}) = (c_b^2 |\bar{\mathbf{q}}|^2 + \Delta_b^2)^{1/2}, \quad (16)$$

where  $\mathbf{q} = \bar{\mathbf{q}} + \mathbf{Q}_{\text{AF}}$ . Above, the velocity of the hidden spinwaves is given by  $c_b = (\rho_s/\chi_\perp)^{1/2}$ , where  $\rho_s$  is the spin stiffness of the hSDW, while the spin gap  $\Delta_b$  is null when the hSDW

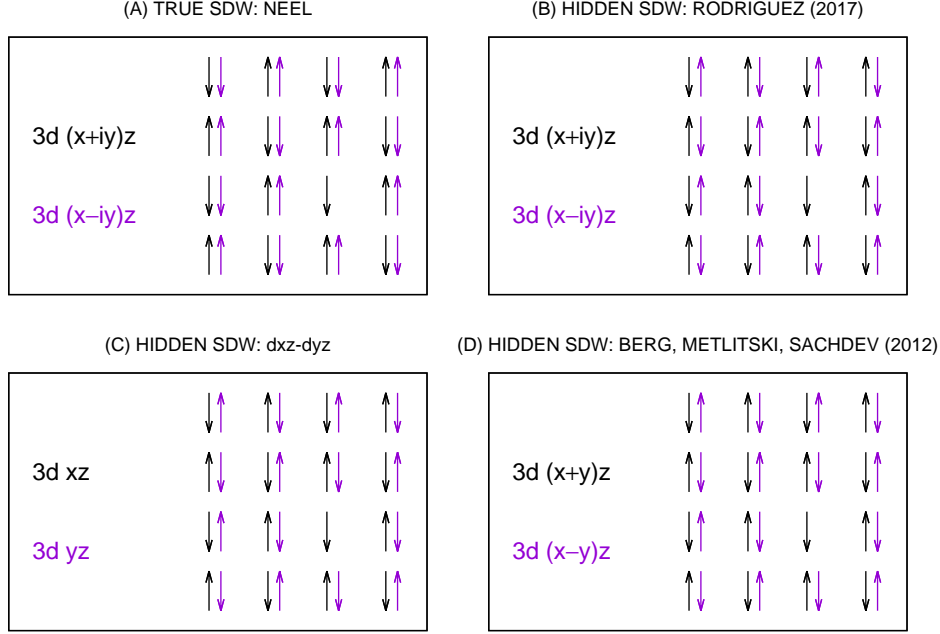


FIG. 3: Spin/orbital configurations for (a) conventional Néel order, and for hidden Néel order among orbitals along (b) the  $I^{(3)}$  isospin axis, along (c) the  $I^{(1)}$  isospin axis, and along (d) the  $I^{(2)}$  isospin axis.

state shows long-range order. It can be demonstrated that the spin  $s_1$  is equal to the spin per orbital in the local-moment limit described by the two-orbital Heisenberg model<sup>34</sup> (74).

### III. ELIASHBERG THEORY

After adding on-iron-site Coulomb repulsion (8) and magnetic frustration from superexchange via the selenium atoms (10) to the electron hopping Hamiltonian (1), the author and Melendrez recently showed that the hSDW state, with opposing Néel antiferromagnet order over the square lattice of iron atoms per  $d_{\pm}$  orbital, is stable within the mean-field approximation at perfect nesting<sup>26</sup>. (See Fig. 1.) And after developing an Eliashberg theory in the particle-hole channel, these authors then showed that coupling to hidden spin fluctuations, (15) and (16), shifts the two electronic bands by an equal and opposite energy, leading to electron/hole Fermi surface pockets at the corner of the folded (two-iron) Brillouin zone. They also notably found that the spectral weight,  $1/Z$ , tends to zero at the new Fermi surface pockets.

Berg, Metlitski and Sachdev have performed determinant quantum Monte Carlo (DQMC) simulations on a similar model<sup>25</sup> that includes weak nesting of Fermi surfaces by the Néel wavevector  $\mathbf{Q}_{\text{AF}}$  and coupling to hidden spin fluctuations with isospin quantum number  $I^{(2)} = 0$ . (See Table IV and Fig. 3d.) They find a quantum-critical phase transition at low temperature between a hSDW and a  $D$ -wave superconductor, with Cooper pairs on nominal  $x$  versus  $y$  orbitals that alternate in sign between them. Below, we will show that a similar quantum-critical phase transition exists upon electron doping of the hSDW state considered here, with isospin quantum number  $I^{(3)} = 0$  instead. In particular, an Eliashberg theory in the conventional particle-particle channel<sup>39–42</sup> will be revealed for electron-doped states that exhibit only short-range hSDW order. It predicts Cooper pairs that show  $S$ -wave symmetry, however.

### A. Hidden Spin Fluctuations and Interaction with Electrons

In the hidden Néel state considered here, with spontaneous symmetry breaking along the  $z$  axis, the propagator for spinwaves is given by

$$\left\langle \frac{1}{\sqrt{2}}m^+(\pi)\frac{1}{\sqrt{2}}m^-(\pi) \right\rangle \Big|_{\mathbf{q},\omega} = iD(\mathbf{q},\omega), \quad (17)$$

with its form set by (15) and (16). We shall henceforth assume that the spin gap  $\Delta_b$  grows in a continuous fashion from zero upon crossing the quantum critical point. Electron doping from half filling shall be one of the principal tuning parameters for the quantum-critical phase transition. (Cf. Fig. 7.) Spin isotropy is recovered upon crossing the quantum critical point, however. It dictates the form

$$\left\langle \frac{1}{\sqrt{2}}m^{(z)}(\pi)\frac{1}{\sqrt{2}}m^{(z)}(\pi) \right\rangle \Big|_{\mathbf{q},\omega} = \frac{1}{2}iD(\mathbf{q},\omega), \quad (18)$$

for the nature of hidden spin fluctuations along the  $z$  axis at  $\Delta_b > 0$ .

As was mentioned earlier, the extended Hubbard model over the square lattice of iron atoms in FeSe that was introduced in subsection II B at perfect nesting of the Fermi surfaces (Fig. 1) harbors a hSDW state when magnetic frustration is present<sup>26</sup>. A mean field theory approximation of the extended Hubbard model implies an isotropic interaction between spin fluctuations and electrons of the form  $H_{\text{e-hsw}} = -\sum_i \sum_\alpha U(\pi)\mathbf{m}_{i,\alpha} \cdot 2\mathbf{S}_{i,\alpha}$ , where

$$U(\pi) = U_0 + \frac{1}{2}J_0. \quad (19)$$

Here,  $U_0$  is the on-site repulsive energy cost for the formation of a spin singlet on the  $d+$  orbital or on the  $d-$  orbital, while  $J_0$  is the (ferromagnetic) Hund's Rule spin-exchange coupling constant between these two orbitals. The transverse contributions yield the interaction  $H_{e\text{-hsw}}^{(xy)} = -\sum_i \sum_\alpha U(\pi)(m_{i,\alpha}^+ S_{i,\alpha}^- + m_{i,\alpha}^- S_{i,\alpha}^+)$ , while the longitudinal contributions yield the interaction  $H_{e\text{-hsw}}^{(z)} = -\sum_i \sum_\alpha U(\pi)m_{i,\alpha}^{(z)} 2S_{i,\alpha}^{(z)}$ . In the basis of electron energy bands, they yield the following contribution to the Hamiltonian due to the interaction of electrons with hidden spin fluctuations:

$$H_{e\text{-hsw}}^{(xy)} = -\frac{1}{\sqrt{2}} \frac{U(\pi)}{a\mathcal{N}^{1/2}} \sum_{\mathbf{k}} \sum_{\mathbf{k}'} \sum_n [m^+(\pi, \mathbf{q}) c_{\downarrow}^\dagger(\bar{n}, \bar{\mathbf{k}}') c_{\uparrow}(n, \mathbf{k}) \mathcal{M}_{n,\mathbf{k};\bar{n},\bar{\mathbf{k}}'} + \text{h.c.}] \quad (20)$$

and

$$H_{e\text{-hsw}}^{(z)} = -\frac{1}{\sqrt{2}} \frac{U(\pi)}{a\mathcal{N}^{1/2}} \sum_{\mathbf{k}} \sum_{\mathbf{k}'} \sum_n \sum_s m^{(z)}(\pi, \mathbf{q}) c_s^\dagger(\bar{n}, \bar{\mathbf{k}}') c_s(n, \mathbf{k}) \cdot \mathcal{M}_{n,\mathbf{k};\bar{n},\bar{\mathbf{k}}'}(\text{sgn } s), \quad (21)$$

where  $\mathbf{q} = \mathbf{k} - \bar{\mathbf{k}}'$  is the momentum transfer, with  $\bar{\mathbf{k}}' = \mathbf{k}' + \mathbf{Q}_{\text{AF}}$ . Above,  $c_s^\dagger(n, \mathbf{k})$  and  $c_s(n, \mathbf{k})$  are electron creation and destruction operators for plane-wave states (5). The band indices  $n = 1$  and  $n = 2$  correspond, respectively, to anti-bonding ( $-$ ) planewaves in the  $d_{y(\delta)z}$  orbital and to bonding ( $+$ ) planewaves in the  $d_{x(\delta)z}$  orbital. Also,  $\bar{n}$  denotes the opposite band. The orbital matrix element that appears in (20) and in (21) is given by<sup>26</sup>

$$\mathcal{M}_{n,\mathbf{k};\bar{n},\bar{\mathbf{k}}'} = \pm \sin[\delta(\mathbf{k}) + \delta(\mathbf{k}')]. \quad (22)$$

(See Appendix B.) Above, intra-band transitions are neglected because they do not show nesting.

We shall now apply the Nambu-Gorkov formalism for paired states<sup>41–44</sup>. It then becomes useful to write the above electron-hidden-spinwave interactions in terms of spinors:

$$H_{e\text{-hsw}}^{(xy)} = \mp \frac{1}{\sqrt{2}} \frac{U(\pi)}{a\mathcal{N}^{1/2}} \sum_{\mathbf{k}} \sum_{\mathbf{k}'} [m^+(\pi, \mathbf{q}) C_n^\dagger(\bar{\mathbf{k}}') \tau_3 \bar{C}_{\bar{n}}(\mathbf{k}) \sin[\delta(\mathbf{k}) + \delta(\mathbf{k}')] + \text{h.c.}], \quad (23)$$

and

$$H_{e\text{-hsw}}^{(z)} = \mp \frac{1}{\sqrt{2}} \frac{U(\pi)}{a\mathcal{N}^{1/2}} \sum_{\mathbf{k}} \sum_{\mathbf{k}'} \sum_n m^{(z)}(\pi, \mathbf{q}) C_{\bar{n}}^\dagger(\bar{\mathbf{k}}') \tau_0 C_n(\mathbf{k}) \cdot \sin[\delta(\mathbf{k}) + \delta(\mathbf{k}')], \quad (24)$$

with

$$C_n(\mathbf{k}) = \begin{bmatrix} c_\uparrow(n, \mathbf{k}) \\ c_\downarrow^\dagger(n, -\mathbf{k}) \end{bmatrix} \quad (25)$$

and

$$\bar{C}_n(\mathbf{k}) = \begin{bmatrix} c_\downarrow(n, \mathbf{k}) \\ c_\uparrow^\dagger(n, -\mathbf{k}) \end{bmatrix}. \quad (26)$$

Above,  $\tau_3$  is the Pauli matrix along the  $z$  axis, and  $\tau_0$  is the  $2 \times 2$  identity matrix. Also, the explicit matrix element (22)  $\mathcal{M}_{n,\mathbf{k};\bar{n},\bar{\mathbf{k}}}$  has been substituted in. (See Appendix B.) It is important to point out that the band index  $n$  is *fixed* in expression (23) for  $H_{\text{e-hsw}}^{(xy)}$  above. The  $n = 1$  and the  $n = 2$  expressions are equivalent.

## B. Electron Propagators and Eliashberg Equations

Let  $C_n(\mathbf{k}, t)$  and  $\bar{C}_n(\mathbf{k}, t)$  denote the time evolution of the Nambu-Gorkov spinors,  $C_n(\mathbf{k})$  and  $\bar{C}_n(\mathbf{k})$ , and let  $C_n^\dagger(\mathbf{k}, t)$  and  $\bar{C}_n^\dagger(\mathbf{k}, t)$  denote the time evolution of their conjugates,  $C_n^\dagger(\mathbf{k})$  and  $\bar{C}_n^\dagger(\mathbf{k})$ . The Nambu-Gorkov electron propagators are then the Fourier transforms  $iG_n(\mathbf{k}, \omega) = \int dt_{1,2} e^{i\omega t_{1,2}} \langle T[C_n(\mathbf{k}, t_1) C_n^\dagger(\mathbf{k}, t_2)] \rangle$  and  $i\bar{G}_n(\mathbf{k}, \omega) = \int dt_{1,2} e^{i\omega t_{1,2}} \langle T[\bar{C}_n(\mathbf{k}, t_1) \bar{C}_n^\dagger(\mathbf{k}, t_2)] \rangle$ , where  $t_{1,2} = t_1 - t_2$ , and where  $T$  is the time-ordering operator. They are  $2 \times 2$  matrices. In the absence of interactions, their matrix inverses are then given by

$$G_{0n}^{-1}(\mathbf{k}, \omega) = \omega \tau_0 - [\varepsilon_n(\mathbf{k}) - \mu_0] \tau_3. \quad (27)$$

Following the standard prescription<sup>41,42</sup>, let us next assume that the matrix inverse of the Nambu-Gorkov Greens function takes the form

$$G_n^{-1}(\mathbf{k}, \omega) = Z_n(\mathbf{k}, \omega) \omega \tau_0 - [\varepsilon_n(\mathbf{k}) - \mu_n] \tau_3 - Z_n(\mathbf{k}, \omega) \Delta_n(\mathbf{k}) \tau_1. \quad (28)$$

Here,  $Z_n(\mathbf{k}, \omega)$  is the wavefunction renormalization,  $\Delta_n(\mathbf{k})$  is the quasi-particle gap, and  $\mu_n - \mu_0$  is the shift in the energy band. Matrix inversion of (28) yields the Nambu-Gorkov



Greens function<sup>41-44</sup>  $G = \sum_{\mu=0}^3 G^{(\mu)}\tau_{\mu}$ , with components

$$\begin{aligned} G_n^{(0)} &= \frac{1}{2Z_n} \left( \frac{1}{\omega - E_n} + \frac{1}{\omega + E_n} \right), \\ G_n^{(1)} &= \frac{1}{2Z_n} \left( \frac{1}{\omega - E_n} - \frac{1}{\omega + E_n} \right) \frac{\Delta_n}{E_n}, \\ G_n^{(3)} &= \frac{1}{2Z_n} \left( \frac{1}{\omega - E_n} - \frac{1}{\omega + E_n} \right) \frac{\varepsilon_n - \mu_n}{Z_n E_n}, \end{aligned} \quad (29)$$

and  $G_n^{(2)} = 0$ . Above, the excitation energy is

$$E_n(\mathbf{k}, \omega) = \sqrt{\left[ \frac{\varepsilon_n(\mathbf{k}) - \mu_n}{Z_n(\mathbf{k}, \omega)} \right]^2 + \Delta_n^2(\mathbf{k})}. \quad (30)$$

Last, because the spinors (25) and (26) are related by spin flip, and because we assume spin singlet Cooper pairs, then  $\bar{G}$  is obtained from  $G$  by the replacement  $\Delta_n \rightarrow -\Delta_n$ . This yields  $\bar{G}_n^{(0)} = G_n^{(0)}$ ,  $\bar{G}_n^{(1)} = -G_n^{(1)}$ ,  $\bar{G}_n^{(2)} = -G_n^{(2)}$ , and  $\bar{G}_n^{(3)} = G_n^{(3)}$ .

To obtain the Eliashberg equations, recall first the definition of the self-energy correction per band:  $G_n^{-1} = G_0^{-1} - \Sigma_n$ . Comparison of the inverse Greens functions (27) and (28) then yields the following expression for it<sup>41,42</sup>:

$$\Sigma_n(\mathbf{k}, \omega) = [1 - Z_n(\mathbf{k}, \omega)]\omega\tau_0 - (\mu_n - \mu_0)\tau_3 + Z_n(\mathbf{k}, \omega)\Delta_n(\mathbf{k})\tau_1. \quad (31)$$

Next, we neglect vertex corrections from the electron-hidden-spinwave interactions, (23) and (24). Figure 4 displays the resulting self-consistent approximation. This approximation will be justified *a posteriori* in the next section. The self-energy correction is then given by

$$\begin{aligned} \Sigma_n(\mathbf{k}, \omega) &= i \int_{\text{BZ}} \frac{d^2k'}{(2\pi)^2} \int_{-\infty}^{+\infty} \frac{d\omega'}{2\pi} \frac{U^2(\pi)}{2} \sin^2[\delta(\mathbf{k}) + \delta(\mathbf{k}')] D(\mathbf{q}, q_0) \cdot \\ &\quad \cdot [\tau_3 \bar{G}_{\bar{n}}(\bar{\mathbf{k}}', \omega')\tau_3 + \frac{1}{2} G_{\bar{n}}(\bar{\mathbf{k}}', \omega')], \end{aligned} \quad (32)$$

with  $q_0 = \omega - \omega'$ , and with  $\mathbf{q} = \mathbf{k} - \bar{\mathbf{k}}'$ . Observe, finally, that  $\tau_3\tau_{\mu}\tau_3 = \text{sgn}_{\mu}\tau_{\mu}$ , where  $\text{sgn}_0 = +1 = \text{sgn}_3$ , and where  $\text{sgn}_1 = -1 = \text{sgn}_2$ . Identifying expressions (31) and (32) for the self-energy corrections then yields the following self-consistent Eliashberg equations at

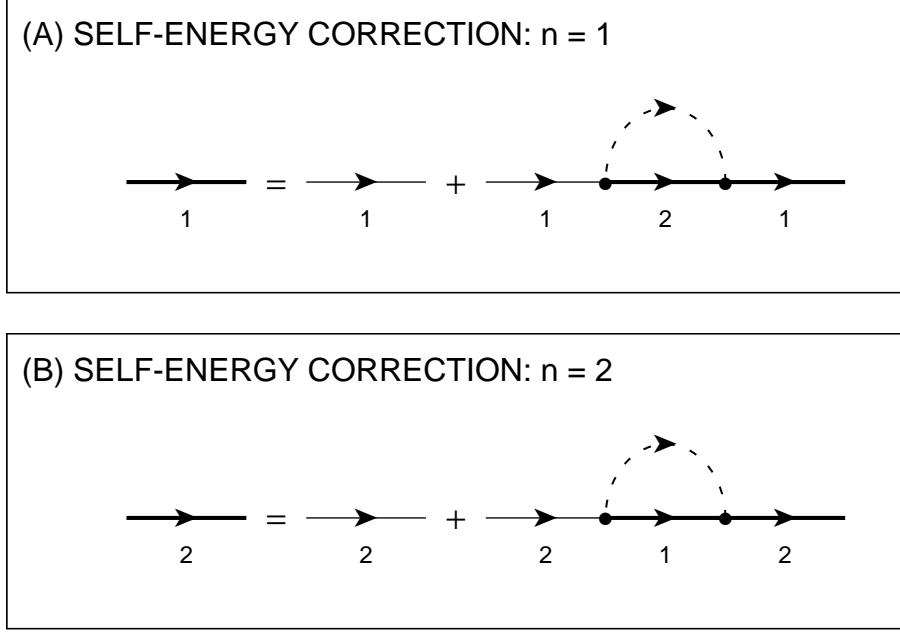


FIG. 4: Feynman diagrams for electron propagator with purely inter-band scattering, in the absence of vertex corrections.

zero temperature:

$$\begin{aligned}
-[Z_n(\mathbf{k}, \omega) - 1]\omega &= + \int_{\text{BZ}} \frac{d^2 k'}{(2\pi)^2} i \int_{-\infty}^{+\infty} \frac{d\omega'}{2\pi} \frac{U^2(\pi)}{2} \sin^2[\delta(\mathbf{k}) + \delta(\mathbf{k}')] \cdot \\
&\quad \cdot D(\mathbf{q}, q_0) [\bar{G}_n^{(0)}(\bar{\mathbf{k}}', \omega') + \frac{1}{2} G_n^{(0)}(\bar{\mathbf{k}}', \omega')], \\
\mu_0 - \mu_n &= + \int_{\text{BZ}} \frac{d^2 k'}{(2\pi)^2} i \int_{-\infty}^{+\infty} \frac{d\omega'}{2\pi} \frac{U^2(\pi)}{2} \sin^2[\delta(\mathbf{k}) + \delta(\mathbf{k}')] \cdot \\
&\quad \cdot D(\mathbf{q}, q_0) [\bar{G}_n^{(3)}(\bar{\mathbf{k}}', \omega') + \frac{1}{2} G_n^{(3)}(\bar{\mathbf{k}}', \omega')], \\
Z_n(\mathbf{k}, \omega) \Delta_n(\mathbf{k}, \omega) &= - \int_{\text{BZ}} \frac{d^2 k'}{(2\pi)^2} i \int_{-\infty}^{+\infty} \frac{d\omega'}{2\pi} \frac{U^2(\pi)}{2} \sin^2[\delta(\mathbf{k}) + \delta(\mathbf{k}')] \cdot \\
&\quad \cdot D(\mathbf{q}, q_0) [\bar{G}_n^{(1)}(\bar{\mathbf{k}}', \omega') - \frac{1}{2} G_n^{(1)}(\bar{\mathbf{k}}', \omega')].
\end{aligned} \tag{33}$$

The Greens functions above are listed in (29) and below (30).

Last, it becomes useful to write the propagator for hidden spinwaves (15) as

$$D(\mathbf{q}, \omega) = \frac{(2s_1)^2}{\chi_{\perp}} \frac{1}{2\omega_b(\mathbf{q})} \left[ \frac{1}{\omega - \omega_b(\mathbf{q})} - \frac{1}{\omega + \omega_b(\mathbf{q})} \right]. \tag{34}$$

The integrals over frequency in the Eliashberg equations above (33) can be evaluated by

going into the complex plane. Specifically, make the replacement  $E_n \rightarrow E_n - i\eta$  in the poles of the electron Greens functions (29), make the replacement  $\omega_b(\mathbf{q}) \rightarrow \omega_b(\mathbf{q}) - i\eta$  in the poles of the spin-wave propagator (34), and regularize the contour integrals by including the factor  $e^{i\omega'\tau}$  in the integrands. Here,  $\eta \rightarrow 0+$  and  $\tau \rightarrow 0+$ . Application of Cauchy's residue theorem yields the following result, which is equivalent to Brillouin-Wigner second-order perturbation theory<sup>41</sup>:

$$\begin{aligned}
[Z_n(\mathbf{k}, \omega) - 1]\omega &= \frac{3}{2} \int_{\text{BZ}} \frac{d^2k'}{(2\pi)^2} U^2(\pi) \frac{s_1^2 \sin^2[\delta(\mathbf{k}) + \delta(\mathbf{k}')] }{\chi_\perp Z_{\bar{n}}(\bar{\mathbf{k}}', \omega')} . \\
&\cdot \frac{1}{2\omega_b(\mathbf{q})} \left[ \frac{1}{\omega_b(\mathbf{q}) + E_{\bar{n}}(\bar{\mathbf{k}}') - \omega} - \frac{1}{\omega_b(\mathbf{q}) + E_{\bar{n}}(\bar{\mathbf{k}}') + \omega} \right], \\
\mu_0 - \mu_n &= -\frac{3}{2} \int_{\text{BZ}} \frac{d^2k'}{(2\pi)^2} U^2(\pi) \frac{s_1^2 \sin^2[\delta(\mathbf{k}) + \delta(\mathbf{k}')] }{\chi_\perp Z_{\bar{n}}(\bar{\mathbf{k}}', \omega')} \frac{\varepsilon_{\bar{n}}(\bar{\mathbf{k}}') - \mu_{\bar{n}}}{Z_{\bar{n}}(\bar{\mathbf{k}}', \omega') E_{\bar{n}}(\bar{\mathbf{k}}')} . \\
&\cdot \frac{1}{2\omega_b(\mathbf{q})} \left[ \frac{1}{\omega_b(\mathbf{q}) + E_{\bar{n}}(\bar{\mathbf{k}}') - \omega} + \frac{1}{\omega_b(\mathbf{q}) + E_{\bar{n}}(\bar{\mathbf{k}}') + \omega} \right], \\
Z_n(\mathbf{k}, \omega) \Delta_n(\mathbf{k}, \omega) &= -\frac{3}{2} \int_{\text{BZ}} \frac{d^2k'}{(2\pi)^2} U^2(\pi) \frac{s_1^2 \sin^2[\delta(\mathbf{k}) + \delta(\mathbf{k}')] }{\chi_\perp Z_{\bar{n}}(\bar{\mathbf{k}}', \omega')} \frac{\Delta_{\bar{n}}(\bar{\mathbf{k}}', \omega')}{E_{\bar{n}}(\bar{\mathbf{k}}')} . \\
&\cdot \frac{1}{2\omega_b(\mathbf{q})} \left[ \frac{1}{\omega_b(\mathbf{q}) + E_{\bar{n}}(\bar{\mathbf{k}}') - \omega} + \frac{1}{\omega_b(\mathbf{q}) + E_{\bar{n}}(\bar{\mathbf{k}}') + \omega} \right].
\end{aligned} \tag{35}$$

Above<sup>42</sup>,  $\omega' = E_{\bar{n}}(\bar{\mathbf{k}}')$ . In the previous, the momentum integrals have been shifted by  $\mathbf{Q}_{\text{AF}}$  for convenience in order to exploit perfect nesting (7). Also, the prefactors of 3/2 above are a result of the identities between  $G_n^{(\mu)}$  and  $\bar{G}_n^{(\mu)}$  that are listed below (30). We shall now find solutions to the Eliashberg equations.

#### IV. LIFSHITZ TRANSITION AND PAIRING INSTABILITY AT THE FERMI SURFACE

Henceforth, assume isotropic ( $S$ -wave) Cooper pairs. Following the standard procedure<sup>41,42</sup>, let us multiply both sides of the Eliashberg equations (35) by  $\delta[\varepsilon_n(\mathbf{k}) - \mu_n]/D_n(\mu_n)$  and integrate in momentum over the first Brillouin zone. The Eliashberg equa-

tions (35) thereby reduce to

$$(Z_n - 1)\omega = \int_{-W_{\text{bottom}}(\bar{n})}^{+W_{\text{top}}(\bar{n})} d\varepsilon' Z_{\bar{n}}^{-1} \int_0^\infty d\Omega U^2 F_0^{(n,\bar{n})}(\Omega; \mu_n, \mu_{\bar{n}}) \cdot \frac{1}{2} \left[ \frac{1}{\Omega + E'_{\bar{n}} - \omega} - \frac{1}{\Omega + E'_{\bar{n}} + \omega} \right], \quad (36a)$$

$$\mu_0 - \mu_n = - \int_{-W_{\text{bottom}}(\bar{n})}^{+W_{\text{top}}(\bar{n})} d\varepsilon' Z_{\bar{n}}^{-1} \int_0^\infty d\Omega U^2 F_0^{(n,\bar{n})}(\Omega; \mu_n, \mu_{\bar{n}}) \frac{\varepsilon' - \mu_{\bar{n}}}{Z'_{\bar{n}} E'_{\bar{n}}} \cdot \frac{1}{2} \left[ \frac{1}{\Omega + E'_{\bar{n}} - \omega} + \frac{1}{\Omega + E'_{\bar{n}} + \omega} \right], \quad (36b)$$

$$Z_n \Delta_n = - \int_{-W_{\text{bottom}}(\bar{n})}^{+W_{\text{top}}(\bar{n})} d\varepsilon' Z_{\bar{n}}^{-1} \int_0^\infty d\Omega U^2 F_0^{(n,\bar{n})}(\Omega; \mu_n, \mu_{\bar{n}}) \frac{\Delta'_{\bar{n}}}{E'_{\bar{n}}} \cdot \frac{1}{2} \left[ \frac{1}{\Omega + E'_{\bar{n}} - \omega} + \frac{1}{\Omega + E'_{\bar{n}} + \omega} \right], \quad (36c)$$

where

$$U^2 F_0^{(n,\bar{n})}(\Omega; \varepsilon, \varepsilon') = \frac{1}{D_n(\varepsilon)} \frac{3}{2} \int \frac{d^2 k}{(2\pi)^2} \int \frac{d^2 k'}{(2\pi)^2} U^2(\pi) \frac{s_1^2 \sin^2[\delta(\mathbf{k}) + \delta(\mathbf{k}')] }{\chi_\perp \omega_b(\mathbf{q})} \cdot \delta[\varepsilon_n(\mathbf{k}) - \varepsilon] \delta[\varepsilon_{\bar{n}}(\bar{\mathbf{k}}') - \varepsilon'] \delta[\omega_b(\mathbf{q}) - \Omega], \quad (37)$$

and where

$$E'_{\bar{n}} = [(\varepsilon' - \mu_{\bar{n}})/Z'_{\bar{n}}]^2 + \Delta_{\bar{n}}'^2)^{1/2}.$$

Here, the wavefunction renormalization and the gap are averaged over the new Fermi surface:  $Z_n(\mathbf{k}, \omega) \rightarrow [D_n(\mu_n)]^{-1} (2\pi)^{-2} \int_{\text{BZ}} d^2 k Z_n(\mathbf{k}, \omega) \delta[\varepsilon_n(\mathbf{k}) - \mu_n]$ , and  $Z_n \Delta_n(\mathbf{k}, \omega) \rightarrow [D_n(\mu_n)]^{-1} (2\pi)^{-2} \int_{\text{BZ}} d^2 k Z_n \Delta_n(\mathbf{k}, \omega) \delta[\varepsilon_n(\mathbf{k}) - \mu_n]$ . The neglect of angular dependence is exact for circular Fermi surface pockets at  $(\pi/a, 0)$  and at  $(0, \pi/a)$ . This occurs for  $\mu_2$  near the upper band edge of  $\varepsilon_+(\mathbf{k})$  and for  $\mu_1$  near the lower band edge of  $\varepsilon_-(\mathbf{k})$ , in the absence of nearest-neighbor intra-orbital hopping,  $t_1^\parallel \rightarrow 0$ . Above, we have also approximated the function  $U^2 F_0^{(n,\bar{n})}(\Omega; \mu_n, \varepsilon')$  of  $\varepsilon'$  by its value at the renormalized Fermi level,  $U^2 F_0^{(n,\bar{n})}(\Omega; \mu_n, \mu_{\bar{n}})$ .

## A. Half Filling

One of the central aims of this paper is to reveal a Lifshitz transition from the Fermi surfaces depicted by Fig. 1 to electron/hole pockets at the corner of the folded (two-iron)

Brillouin zone. Let us start at half filling:  $\mu_0 = 0$ . The Fermi surfaces are then set by  $\varepsilon_-(\mathbf{k}) = -\nu$  and  $\varepsilon_+(\mathbf{k}) = +\nu$ , where  $\mu_1 = -\nu$  and  $\mu_2 = +\nu$  are the shifts in energy of the anti-bonding ( $-$ ) band and of the bonding ( $+$ ) band, respectively. Because of perfect nesting (7), we have  $\varepsilon_{\pm}(\bar{\mathbf{k}}) - \mu_{\pm} = \mu_{\mp} - \varepsilon_{\mp}(\mathbf{k})$ . The Eliashberg equations (35) are then symmetric with respect to the permutation of the band indices. We thereby have  $Z_1 = Z_2$  and  $\Delta_1 = -\Delta_2$ . These unknowns, in addition to  $\nu$ , are to be determined by the Eliashberg equations (36a)-(36c).

The effective spectral weight of the hidden spinwaves,  $U^2 F_0^{(2,1)}(\Omega; \mu_2, \mu_1)$ , can be evaluated by choosing coordinates for the momentum of the electron,  $(k_{\parallel}, k_{\perp})$ , that are respectively parallel and perpendicular to the Fermi surface of the bonding band ( $\text{FS}_+$ ):  $\nu = \varepsilon_+(\mathbf{k})$ . And because of perfect nesting (7), it coincides with the Fermi surface of the anti-bonding ( $-$ ) band after the momentum is shifted by  $\mathbf{Q}_{\text{AF}}$ :  $\mathbf{k}' \rightarrow \bar{\mathbf{k}}'$ . (See Figs. 1 and 5.) This yields the intermediate result

$$U^2 F_0^{(2,1)}(\Omega; \mu_2, \mu_1) = \frac{1}{D_+(\nu)} \frac{3}{2} \oint_{\text{FS}_+} \frac{dk_{\parallel}}{(2\pi)^2} \oint_{\text{FS}_+} \frac{dk'_{\parallel}}{(2\pi)^2} U^2(\pi) \frac{s_1^2}{\chi_{\perp}} \frac{1}{\Omega} \cdot \frac{\sin^2[\delta(\mathbf{k}) + \delta(\mathbf{k}')] }{|\mathbf{v}_+(\mathbf{k})||\mathbf{v}_+(\mathbf{k}')|} \delta[\omega_b(\mathbf{q}) - \Omega], \quad (38)$$

where  $\mathbf{v}_+ = \partial\varepsilon_+/\partial\mathbf{k}$  is the group velocity. Yet the dispersion of the spectrum of hidden spinwaves follows  $\omega_b(\mathbf{q}) = \sqrt{c_b^2|\bar{\mathbf{q}}|^2 + \Delta_b^2}$  at the long-wavelength limit. Making the approximation  $|\bar{\mathbf{q}}| \cong |k_{\parallel} - k'_{\parallel}|$  at small momentum transfers then yields the following dependence on frequency for the effective spectral weight:  $U^2 F_0^{(2,1)}(\Omega; \mu_2, \mu_1) = \epsilon_E(\nu)/\sqrt{\Omega^2 - \Delta_b^2}$  for  $\Omega > \Delta_b$ , with a constant pre-factor

$$\epsilon_E(\nu) = \frac{1}{D_+(\nu)} \frac{3}{2} \oint_{\text{FS}_+} \frac{dk_{\parallel}}{(2\pi)^4} U^2(\pi) \frac{s_1^2}{\chi_{\perp}} \frac{[\sin 2\delta(\mathbf{k})]^2}{c_b |\mathbf{v}_+(\mathbf{k})|^2}, \quad (39)$$

while  $U^2 F_0^{(2,1)}(\Omega; \mu_2, \mu_1) = 0$  for  $0 \leq \Omega \leq \Delta_b$ .

Next, let us assume the trivial solution for the gap equations (36c):  $\Delta_n = 0$ . It will be shown *a posteriori* that this is indeed the case. We can now find solutions to the remaining Eliashberg equations (36a) and (36b). In particular, assume that the equal and opposite shift in energy  $\nu$  of the bands lies near the upper edge  $W_{\text{top}}$  of the bonding band  $\varepsilon_+(\mathbf{k})$  at  $(\pi/a, 0)$  and at  $(0, \pi/a)$ . (Cf. Fig. 2.) Figure 5 displays the Fermi surfaces in such case. Substituting in the previous result for the dependence on frequency of  $U^2 F_0^{(2,1)}(\Omega; \mu_2, \mu_1)$

yields the first Eliashberg equation:

$$\omega(Z - 1) = \frac{\epsilon_E}{2} \int_{\Delta_b}^{\omega_{uv}} \frac{d\Omega}{\sqrt{\Omega^2 - \Delta_b^2}} \ln \left| \frac{\Omega + \omega}{\Omega - \omega} \cdot \frac{W/Z + \Omega - \omega}{W/Z + \Omega + \omega} \right|. \quad (40)$$

Here, we have reversed the order of integration:  $[-W_{\text{bottom}}, +W_{\text{top}}]$  is the range of integration over  $\varepsilon'$  in (36a), where  $-W_{\text{bottom}}$  and  $+W_{\text{top}}$  denote the minimum and the maximum of the band  $\varepsilon_+(\mathbf{k})$ , respectively. Its bandwidth is then  $W = W_{\text{bottom}} + W_{\text{top}}$ . Also,  $\omega_{uv}$  is an ultra-violet cutoff in frequency for the hidden spinwaves. Expanding the integrand above to linear order in frequency  $\omega$  then yields ultimately the Eliashberg equation for the wavefunction renormalization at the Fermi level,  $\omega = 0$ :

$$Z - 1 = \epsilon_E \int_{\Delta_b}^{\omega_{uv}} \frac{d\Omega}{\sqrt{\Omega^2 - \Delta_b^2}} \left( \frac{1}{\Omega} - \frac{1}{W/Z + \Omega} \right). \quad (41)$$

Likewise, inverting the order of integration of the second Eliashberg equation (36b) for the inter-band energy shift yields

$$\nu = \epsilon_E \int_{\Delta_b}^{\omega_{uv}} \frac{d\Omega}{\sqrt{\Omega^2 - \Delta_b^2}} \ln \left| \frac{W/Z + \Omega}{\Omega} \right| \quad (42)$$

at  $\omega = 0$ .

Long-range hSDW order exists at half filling because of perfect nesting (Fig. 5). We must therefore approach criticality:  $\Delta_b \rightarrow 0$ . The Eliashberg equations (41) and (42) predict a Lifshitz transition of the topology of the Fermi surface that is confirmed by making the following change of variables:  $Z = \varepsilon_E/\Delta_b$  and  $\cosh x = \Omega/\Delta_b$ . At criticality,  $\Delta_b \rightarrow 0$ , they yield Eliashberg equations

$$\frac{\varepsilon_E}{W} = \frac{\epsilon_E}{W} [I(0) - I(y)] \quad \text{and} \quad \frac{\nu}{W} = \frac{\epsilon_E}{W} J(y), \quad (43)$$

where

$$I(y) = \int_0^\infty dx \frac{1}{y + \cosh x}, \quad (44a)$$

$$J(y) = \int_0^\infty dx \ln \left( 1 + \frac{y}{\cosh x} \right), \quad (44b)$$

with  $y = W/\varepsilon_E$ . The quadratic dependence of  $\epsilon_E$  on Hubbard repulsion (39) implies that  $\nu$  saturates to  $W_{\text{top}}$  as  $U(\pi)$  diverges. (See Fig. 5.) Dividing the two Eliashberg equations (43), we then get the transcendental equation

$$y^{-1} \frac{W}{W_{\text{top}}} = \frac{I(0) - I(y)}{J(y)} \quad (45)$$

as  $U(\pi) \rightarrow \infty$ . Notice that  $y$  depends only on  $W/W_{\text{top}} = (t_1^{\parallel} + t_1^{\perp})/t_1^{\perp}$  in such case. The definite integrals (44a) and (44b) can be evaluated in closed form. (See Appendix C.) Numerical solutions to the transcendental equation (45) are listed in Table VI.

Last, what is the energy gap of the superconducting state at half filling, approaching criticality? Again, the antisymmetry displayed by the gap equations (36c) at half filling with respect to the permutation of band indices implies perfect  $S^{+-}$  Cooper pairing:  $\Delta_1 = +\Delta$  and  $\Delta_2 = -\Delta$ . (Cf. refs.<sup>45, 46, 47</sup> and<sup>48</sup>.) The last Eliashberg equation (36c) then reads

$$Z\Delta = \int_{-W_{\text{bottom}}}^{+W_{\text{top}}} d\varepsilon' Z^{-1} \frac{\Delta'}{E'} \int_{\Delta_b}^{\omega_{\text{uv}}} d\Omega \frac{\epsilon_{\text{E}}}{\sqrt{\Omega^2 - \Delta_b^2}} \frac{1}{\Omega + E'} \quad (46)$$

at the Fermi level,  $\omega = 0$ , where  $E' = \sqrt{[(\varepsilon' - \nu)/Z]^2 + \Delta'^2}$ . After again making the change of variable  $\Omega = \Delta_b \cosh(x)$ , the first integral over  $\Omega$  in (46) becomes

$$\lim_{\Delta_b \rightarrow 0} \int_0^{\infty} dx \frac{\epsilon_{\text{E}}}{\Delta_b} \left[ \sqrt{\left(\frac{\varepsilon' - \nu}{\varepsilon_{\text{E}}}\right)^2 + \left(\frac{\Delta'}{\Delta_b}\right)^2} + \cosh x \right]^{-1} = \frac{\epsilon_{\text{E}}}{\Delta'} \ln\left(2\frac{\Delta'}{\Delta_b}\right).$$

Here we have used  $\lim_{y \rightarrow \infty} I(y) = y^{-1} \ln(2y)$ . (See Appendix C.) Assume now the simple Bardeen-Cooper-Schrieffer (BCS) form for the frequency dependence of the gap<sup>41</sup>:

$$\Delta(\omega) = \begin{cases} \Delta_0 & \text{for } |\omega| < \omega_c, \\ 0 & \text{otherwise,} \end{cases} \quad (47)$$

but in the limit  $\omega_c \rightarrow 0$ . It is therefore consistent with the previous solutions for  $Z$  and for  $\nu$  in the normal state. The second integral over  $\varepsilon'$  in the gap equation (46) then becomes

$$\Delta_0 \int_{-\omega_c}^{+\omega_c} d\omega' (\omega'^2 + \Delta_0^2)^{-1/2} = 2\Delta_0 \sinh^{-1}\left(\frac{\omega_c}{\Delta_0}\right).$$

Here, we have made the change of variable  $\omega' = (\varepsilon' - \nu)/Z$ . Substituting in the form of the wavefunction renormalization  $Z = \varepsilon_{\text{E}}/\Delta_b$  into the left-hand side of the gap equation (46) plus some manipulation then yields

$$\frac{\Delta_0}{\sinh^{-1}\left(\frac{\omega_c}{\Delta_0}\right)} = \lim_{\Delta_b \rightarrow 0} 2 \frac{\epsilon_{\text{E}}}{\varepsilon_{\text{E}}} \Delta_b \ln\left(2\frac{\Delta_0}{\Delta_b}\right) = 0.$$

As expected, we therefore have a null gap due to superconductivity,  $\Delta_0 = 0$ , at half filling, at criticality.

Finally, the Eliashberg energy scale  $\epsilon_{\text{E}}$  can be easily estimated in the case of small circular renormalized Fermi surface pockets<sup>26</sup>, which occurs as  $t_1^{\parallel} \rightarrow 0$ . In such case, it becomes

convenient to re-express (39) as

$$\epsilon_E(\nu) = \frac{3}{(2\pi)^3} \frac{U^2}{D_+(\nu)} \frac{s_1^2 k_F}{\chi_\perp c_b v_F^2}, \quad (48)$$

where  $U^2$  is the product of  $U^2(\pi)$  with the average of  $\sin^2(2\delta)$  around the hole-type Fermi surface pockets shown in Fig. 5. Here,  $k_F$  and  $v_F$  are the Fermi wavenumber and the Fermi velocity, respectively. They are given by  $k_F = a^{-1}(2\pi x_0)^{1/2}$ , where  $x_0$  denotes the concentration of electrons/holes in each Fermi surface pocket, and by  $v_F = 2t_1^\perp a^2 k_F$ . The solution to the Eliashberg equations (43) yields  $\epsilon_E \cong W/3$ . (See Table VI.) Expression (48) then implies that the effective interaction strength scales as  $U \propto x_0^{1/4}$ . Further, expression (6b) yields the result  $\sin 2\delta(\mathbf{k}) \cong [(t_2^\perp/i)/2t_1^\perp](k_F a)^2 (\sin 2\phi)$ , where  $\phi$  is the angle that  $\mathbf{k}$  makes about the center of the Fermi surface pocket. The Eliashberg energy scale is thereby given explicitly by the following expression at criticality<sup>26</sup>, as  $t_1^\parallel \rightarrow 0$ :

$$\epsilon_E = \frac{3}{32} \left( \frac{x_0}{2\pi} \right)^{3/2} \frac{U^2(\pi)}{a^2 D_+(\nu)} \frac{s_1^2}{a^2 \chi_\perp} \frac{|t_2^\perp|^2}{(c_b/a) |t_1^\perp|^4}. \quad (49)$$

The solution  $\epsilon_E \cong W/3$  listed in Table VI then yields that the area of the electron/hole Fermi surface pockets shown in Fig. 5 is related to the Hubbard repulsion by  $U(\pi) \propto x_0^{-3/4}$ . We therefore conclude that the effective interaction strength  $U$  vanishes with the strength of the Hubbard repulsion<sup>26</sup> as  $U(\pi)^{-1/3}$ . In the case where the spectrum  $\omega_b(\mathbf{q})$  of hidden spin fluctuations is *fixed*, this justifies the neglect of vertex corrections to the self-energy corrections shown by Fig. 4 at large Hubbard repulsion,  $U(\pi) \rightarrow \infty$ .

As on-site repulsion  $U_0$  grows strong, the Eliashberg equations (36a)-(36c) therefore predict a Lifshitz transition from unrenormalized Fermi surfaces shown in Fig. 1 to renormalized Fermi surface pockets shown in Fig. 5. The groundstate remains an hSDW at half filling due to nested Fermi surface pockets at the corner of the folded Brillouin zone. It must be emphasized, however, that the spectral weight of the renormalized Fermi surface pockets is vanishingly small:  $Z^{-1} = \Delta_b/\epsilon_E \rightarrow 0$  at criticality,  $\Delta_b \rightarrow 0$ . This implies that the hSDW state at half filling is in fact a Mott insulator. It is also important to mention that these results for the Lifshitz transition confirm previous ones that start from the other side of the QCP at  $\Delta_b = 0$ . They were based on an Eliashberg theory in the particle-hole channel for the long-range ordered hSDW state<sup>26</sup>.



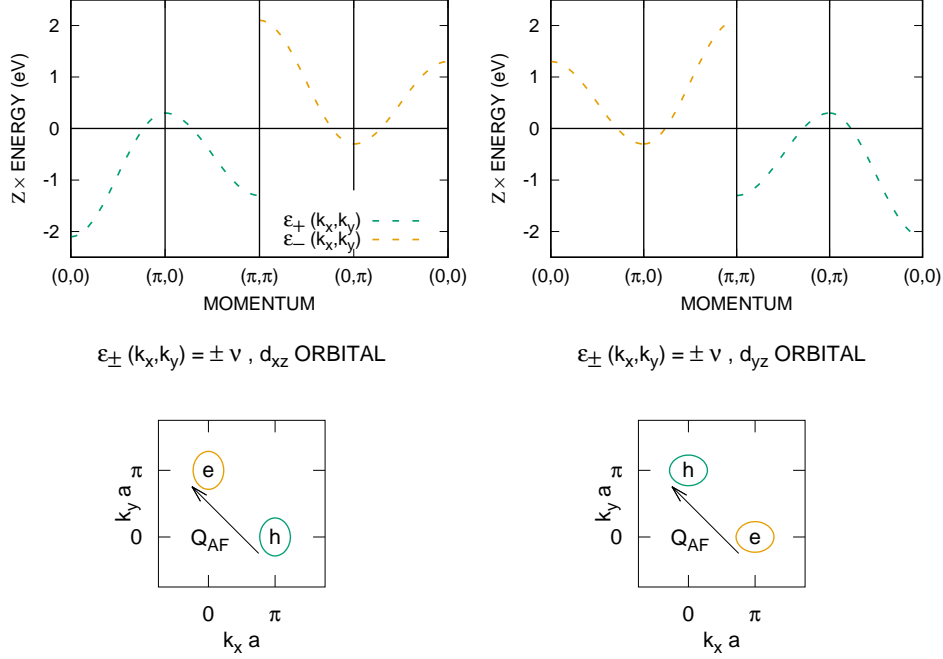


FIG. 5: Renormalized electron bands and Fermi surfaces at half filling after the Lifshitz transition from Fig. 1. The staggered band shift is  $\nu = 1.7$  eV. The orbital character is only approximate, although it becomes exact as the area of the Fermi surface pockets vanishes as  $U(\pi)$  diverges.

## B. Weak Electron Doping

We will now obtain solutions to the Eliashberg equations (35) at small deviations in the electron density from half filling. In the normal state,  $\Delta_1 = 0 = \Delta_2$ , the corresponding equations for the wavefunction renormalizations and for the band shifts read

$$Z_n - 1 = \frac{3}{2} \int \frac{d^2 k'}{(2\pi)^2} U^2(\pi) \frac{s_1^2 \sin^2[\delta(\mathbf{k}) + \delta(\mathbf{k}')] }{\chi_\perp Z_{\bar{n}} \omega_b(\mathbf{q})} \cdot \frac{1}{[\omega_b(\mathbf{q}) + |\varepsilon_+(\mathbf{k}') - \nu_{\bar{n}}|/Z_{\bar{n}}]^2}, \quad (50a)$$

$$\nu_n - (\text{sgn } n)\mu_0 = \frac{3}{2} \int \frac{d^2 k'}{(2\pi)^2} U^2(\pi) \frac{s_1^2 \sin^2[\delta(\mathbf{k}) + \delta(\mathbf{k}')] }{\chi_\perp Z_{\bar{n}} \omega_b(\mathbf{q})} \cdot \frac{\text{sgn}[\nu_{\bar{n}} - \varepsilon_+(\mathbf{k}')] }{\omega_b(\mathbf{q}) + |\varepsilon_+(\mathbf{k}') - \nu_{\bar{n}}|/Z_{\bar{n}}}. \quad (50b)$$

Above,  $\nu_1 = -\mu_1$  and  $\nu_2 = +\mu_2$  are the staggered band shifts. Also, the identity

$$\sin[\delta(\mathbf{k}) + \delta(\mathbf{k}')] = \sin[\delta(\bar{\mathbf{k}}) + \delta(\bar{\mathbf{k}}')] \quad (51)$$

has been applied above in the case  $n = 1$  for the anti-bonding ( $-$ ) band. (See Appendix B.) Assume, in particular, that the chemical potential is positive, but small:  $\mu_0 \rightarrow 0+$ . Assume,

next, a linear response  $\delta Z_1$  and  $\delta Z_2$  with respect to the wavefunction renormalization at half filling,  $Z_1 = Z$  and  $Z_2 = Z$ , along with a linear response  $\delta\nu_1$  and  $\delta\nu_2$  with respect to the staggered band shifts at half filling,  $\nu_1 = \nu$  and  $\nu_2 = \nu$ . Taking a variation of (50a) yields one linear equation per band,  $n = 1, 2$ . Adding and subtracting these yields the following linear relations in terms of even and odd variations with respect to half filling:

$$\begin{aligned} Z \delta Z(+) &= A \delta Z(+) - B \delta\nu(+), \\ 0 &= A \delta Z(-) - B \delta\nu(-), \end{aligned} \quad (52)$$

where  $\delta Z(\pm) = \frac{1}{2}(\delta Z_2 \pm \delta Z_1)$  and  $\delta\nu(\pm) = \frac{1}{2}(\delta\nu_2 \pm \delta\nu_1)$ . Here, we have constants

$$\begin{aligned} A &= \frac{3}{2} \int \frac{d^2 k'}{(2\pi)^2} U^2(\pi) \frac{s_1^2 \sin^2[\delta(\mathbf{k}) + \delta(\mathbf{k}')] }{\chi_\perp \omega_b(\mathbf{q})} \frac{1}{Z} \frac{|\varepsilon_+(\mathbf{k}') - \nu|/Z}{[\omega_b(\mathbf{q}) + |\varepsilon_+(\mathbf{k}') - \nu|/Z]^3}, \\ B &= \frac{3}{2} \int \frac{d^2 k'}{(2\pi)^2} U^2(\pi) \frac{s_1^2 \sin^2[\delta(\mathbf{k}) + \delta(\mathbf{k}')] }{\chi_\perp \omega_b(\mathbf{q})} \frac{1}{Z} \frac{\text{sgn}[\nu - \varepsilon_+(\mathbf{k}')] }{[\omega_b(\mathbf{q}) + |\varepsilon_+(\mathbf{k}') - \nu|/Z]^3}. \end{aligned} \quad (53)$$

Likewise, taking a variation of (50b) yields a second linear equation per band,  $n = 1, 2$ . Adding and subtracting these as well yields two more linear relations in terms of even and odd variations with respect to half filling:

$$\begin{aligned} \nu \delta Z(+) + Z \delta\nu(+) &= (E - C) \delta\nu(+) + D \delta Z(+), \\ Z \mu_0 + \nu \delta Z(-) - Z \delta\nu(-) &= (E - C) \delta\nu(-) + D \delta Z(-). \end{aligned} \quad (54)$$

Here, we have constants

$$\begin{aligned} C &= \frac{3}{2} \int \frac{d^2 k'}{(2\pi)^2} U^2(\pi) \frac{s_1^2 \sin^2[\delta(\mathbf{k}) + \delta(\mathbf{k}')] }{\chi_\perp \omega_b(\mathbf{q})} \frac{1}{Z} \frac{1}{[\omega_b(\mathbf{q}) + |\varepsilon_+(\mathbf{k}') - \nu|/Z]^2}, \\ D &= \frac{3}{2} \int \frac{d^2 k'}{(2\pi)^2} U^2(\pi) \frac{s_1^2 \sin^2[\delta(\mathbf{k}) + \delta(\mathbf{k}')] }{\chi_\perp \omega_b(\mathbf{q})} \frac{1}{Z} \frac{\text{sgn}[\nu - \varepsilon_+(\mathbf{k}')] |\varepsilon_+(\mathbf{k}') - \nu|/Z}{[\omega_b(\mathbf{q}) + |\varepsilon_+(\mathbf{k}') - \nu|/Z]^2}, \end{aligned} \quad (55)$$

and

$$E = \frac{3}{2} \int \frac{d^2 k'}{(2\pi)^2} U^2(\pi) \frac{s_1^2 \sin^2[\delta(\mathbf{k}) + \delta(\mathbf{k}')] }{\chi_\perp \omega_b(\mathbf{q})} \frac{2 \delta[\nu - \varepsilon_+(\mathbf{k}')] }{\omega_b(\mathbf{q}) + |\varepsilon_+(\mathbf{k}') - \nu|/Z}. \quad (56)$$

Collecting terms in (52) and in (54), we get

$$\delta Z(+) = -\frac{B}{F} \delta\nu(+) \quad \text{and} \quad \delta Z(+) = -\frac{2Z - E}{G} \delta\nu(+) \quad (57)$$

in the even channel, and we get

$$\delta Z(-) = \frac{B}{A} \delta \nu(-) \quad \text{and} \quad Z \mu_0 = E \delta \nu(-) - G \delta Z(-) \quad (58)$$

in the odd channel, where  $F = Z - A$  and  $G = \nu - D$ . These constants are then

$$F = \frac{3}{2} \int \frac{d^2 k'}{(2\pi)^2} U^2(\pi) \frac{s_1^2 \sin^2[\delta(\mathbf{k}) + \delta(\mathbf{k}')] }{\chi_\perp Z} \frac{1}{[\omega_b(\mathbf{q}) + |\varepsilon_+(\mathbf{k}') - \nu|/Z]^3}, \quad (59)$$

$$G = \frac{3}{2} \int \frac{d^2 k'}{(2\pi)^2} U^2(\pi) \frac{s_1^2 \sin^2[\delta(\mathbf{k}) + \delta(\mathbf{k}')] }{\chi_\perp Z} \frac{\text{sgn}[\nu - \varepsilon_+(\mathbf{k}')] }{[\omega_b(\mathbf{q}) + |\varepsilon_+(\mathbf{k}') - \nu|/Z]^2}. \quad (60)$$

In deriving expression (59), the first Eliashberg equation (50a) at half filling  $Z - 1 = C$  has been approximated by  $Z = C$ . This is exact at criticality,  $\Delta_b \rightarrow 0$ . And in deriving expression (60), the second Eliashberg equation (50b) for  $\nu$  at half filling has been applied.

We shall now evaluate the constants above that determine the linear response of the Eliashberg equations in the normal state driven by weak electron doping with respect to half filling: (50a) and (50b), as  $\mu_0 \rightarrow 0+$ . Criticality is again assumed at half filling:  $\Delta_b \rightarrow 0$ . Let us begin by evaluating the constant  $G$  (60). First, average it over the Fermi surface:  $G \rightarrow [D_+(\nu)]^{-1} (2\pi)^{-2} \int_{\text{BZ}} d^2 k G \delta[\varepsilon_+(\mathbf{k}) - \nu]$ . Second, replace the integrals over momentum with the product of  $\Omega$  and the spectral density (37) at half filling:  $U^2 F_0(\Omega) = \epsilon_E / \sqrt{\Omega^2 - \Delta_b^2}$  for  $\Omega > \Delta_b$ , and  $U^2 F_0(\Omega) = 0$  otherwise. This yields

$$G = \int_{\Delta_b}^{\omega_{\text{uv}}} d\Omega \frac{\epsilon_E}{\sqrt{\Omega^2 - \Delta_b^2}} \Omega \int_{-W_{\text{bottom}}}^{+W_{\text{top}}} d\varepsilon' Z^{-1} \frac{\text{sgn}(\nu - \varepsilon')}{[\Omega + |\varepsilon' - \nu|/Z]^2}. \quad (61)$$

Third, perform the first integral over the energy band  $\varepsilon_+(\mathbf{k})$  in the limit of strong on-site repulsion,  $U(\pi) \rightarrow \infty$ , in which case  $\nu$  approaches the top of the band,  $W_{\text{top}}$ . It is equal to  $\Omega^{-1} - (W/Z + \Omega)^{-1}$ . Fourth, make the change of variable  $\Omega = \Delta_b \cosh(x)$  and take the limit  $\Delta_b \rightarrow 0$ . This yields  $G = \epsilon_E y I(y)$ , where  $I(y)$  is the definite integral (44a), with  $y = W/\epsilon_E$ . A closed-form expression for  $I(y)$  is obtained in Appendix C.

The remaining constants can be evaluated in a similar way. In particular, applying the same set of steps above to the expression for the constant  $F$  (59) yields the definite integral

$$F = \frac{1}{2} \frac{\epsilon_E}{\Delta_b} \int_0^\infty dx \frac{1}{\cosh x} \left[ 1 - \frac{1}{(1 + y \text{sech } x)^2} \right] \quad (62)$$

at criticality,  $\Delta_b \rightarrow 0$ , where  $y = W/\epsilon_E$ . It is shown in Appendix C that (62) reduces to the closed-form expression  $F = \frac{1}{2} (\epsilon_E/\Delta_b) [\frac{\pi}{2} - I(y) - y I'(y)]$ , where  $I'(y)$  denotes the derivative

| response/variation | $\delta Z$   | $\delta\nu$   |
|--------------------|--|---|
| $\delta Z$         | $A = \frac{\epsilon_E}{\Delta_b} - F$ with $F = \frac{1}{2} \frac{\epsilon_E}{\Delta_b} [\frac{\pi}{2} - I(y) - yI'(y)]$ | $B = \frac{1}{2} \frac{\epsilon_E}{\Delta_b^2} [I'(y) - I'(0)]$ |
| $\delta\nu$        | $D = \nu - G$ with $G = \epsilon_E y I(y)$   | $E = \pi \frac{\epsilon_E}{\Delta_b}$                           |

TABLE V: Coefficients of the linear response to weak electron doping of the Eliashberg equations (50a) and (50b), at criticality  $\Delta_b \rightarrow 0$ : Eqs. (52) and (54). A closed form expression for the definite integral  $I(y)$  is given in Appendix C, where  $y = W/\epsilon_E$ .

of  $I(y)$ . Likewise, performing the same set of steps on the expression for the constant  $B$  (53) yields the definite integral

$$B = \frac{1}{2} \frac{\epsilon_E}{\Delta_b^2} \int_0^\infty dx \left[ \frac{1}{(\cosh x)^2} - \frac{1}{(y + \cosh x)^2} \right] \quad (63)$$

at criticality. Comparison with the definite integral (44a) therefore yields the expression  $B = \frac{1}{2} (\epsilon_E/\Delta_b^2) [I'(y) - I'(0)]$ . And recall that a closed-form expression for the constant  $A$  is obtained from that for  $F$  above through the identity  $A = Z - F$ . Last, performing the same set of steps on the expression for the constant  $E$  (56) yields the definite integral

$$E = 2 \frac{\epsilon_E}{\Delta_b} \int_0^\infty dx \frac{1}{\cosh x} = \pi \frac{\epsilon_E}{\Delta_b} \quad (64)$$

at criticality. This completes the evaluation of the constants that determine the linear response of the renormalized electronic structure shown in Fig. 5 to weak electron doping at criticality,  $\Delta_b \rightarrow 0$ .

In conclusion, at weak electron doping, the normal-state Eliashberg equations (50a) and (50b) yield independent linear-response equations in the even and in the odd channels, (57) and (58). The coefficients of the linear response are summarized by Table V. In the even channel, we thereby get  $\delta Z(+)=0$  and  $\delta\nu(+)=0$  if  $BG \neq (2Z - E)F$ . Notice that  $B$ ,  $G$  and  $F$  are positive, while  $2Z - E = (2\epsilon_E - \pi\epsilon_E)/\Delta_b$  is negative by Table VI. The former inequality is therefore valid, and we get  $\delta Z_1 = -\delta Z_2$  and  $\delta\mu_1 = \delta\mu_2$ . And in the odd channel, (58) yields

$$\delta Z(-) = \chi_E \frac{B}{A} \mu_0 \quad \text{and} \quad \delta\nu(-) = \chi_E \mu_0, \quad (65)$$

with susceptibility  $\chi_E = Z/(E - \frac{BG}{A})$ . The latter can be calculated from the previous closed-form expressions for the constants  $A$  thru  $G$  that are listed in Table V, and the results are listed in Table VI. Importantly,  $\chi_E$  is positive at  $W/W_{\text{top}}$  between 1.0 and 1.5,

| $W/W_{\text{top}}$ | $\varepsilon_{\text{E}}/W$ | $\epsilon_{\text{E}}/W$ | $\chi_{\text{E}}$ | $X_{\text{E}}W$ |
|--------------------|----------------------------|-------------------------|-------------------|-----------------|
| 1.0                | 0.343                      | 0.366                   | 2.045             | 8.671           |
| 1.1                | 0.298                      | 0.303                   | 2.120             | 9.673           |
| 1.2                | 0.261                      | 0.255                   | 2.200             | 10.780          |
| 1.3                | 0.231                      | 0.218                   | 2.284             | 12.001          |
| 1.4                | 0.206                      | 0.189                   | 2.373             | 13.344          |
| 1.5                | 0.185                      | 0.165                   | 2.467             | 14.821          |

TABLE VI: Numerical solutions of Eliashberg equations at half filling, at criticality, in the limit  $U(\pi) \rightarrow \infty$ : Eq. (45). Also listed are the susceptibilities about half filling:  $\delta\mu_1 = \chi_{\text{E}}\mu_0 = \delta\mu_2$  and  $\delta Z_2/Z = X_{\text{E}}\mu_0 = -\delta Z_1/Z$ . Note that  $W/W_{\text{top}} = 1 + (t_1^{\parallel}/t_1^{\perp})$ .

which corresponds to at most weak eccentricity in the electron/hole Fermi surface pockets at the corner of the two-iron Brillouin zone. Recall that  $\delta\nu(-) = \frac{1}{2}(\delta\mu_1 + \delta\mu_2)$  is the average chemical-potential shift, which is equal to  $\delta\mu_1 = \delta\mu_2$ . The latter and (65) therefore imply a *rigid shift* of the renormalized electronic structure at half filling by a chemical-potential shift proportional to the electron doping. Figure 6 is such a rigid shift of Fig. 5. Also recall that  $\delta Z(-) = \frac{1}{2}(\delta Z_2 - \delta Z_1)$ , which is equal to  $\delta Z_2 = -\delta Z_1$ . Upon electron doping, the latter and (65) imply, on the other hand, that the wavefunction renormalization increases with respect to  $Z = \varepsilon_{\text{E}}/\Delta_b$  on the hole Fermi surface pockets ( $n = 2$ ), while that it decreases with respect to  $Z$  on the electron Fermi surface pockets ( $n = 1$ ). The magnitude of the equal and opposite variation in the wavefunction renormalization is best stated as  $\delta Z(-)/Z = X_{\text{E}}\mu_0$ , where  $X_{\text{E}} = \frac{B}{A}/(E - \frac{BG}{A})$ . The values of  $X_{\text{E}}W$  listed in Table VI suggest that  $Z_1 \gtrsim 1$  and that  $Z_2 \sim 2Z$  at electron doping greater than  $x_0$ . This will be discussed at length below and in the next section.

Yet what is the superconducting gap at weak electron doping with respect to half filling? Inspection of the gap equations in the Eliashberg equations (35) yields that they are equivalent to the ones *at* half filling to linear order in the variations  $\delta Z_1$ ,  $\delta Z_2$ ,  $\delta\mu_1$  and  $\delta\mu_2$ , and in the gaps  $\Delta_1$  and  $\Delta_2$ . Because  $\Delta_1$  and  $\Delta_2$  are null at half filling, the *linear* susceptibility of these quantities with electron doping  $\mu_0 > 0$  is also null. Any superconducting gap that opens at weak electron doping must therefore depend non-linearly on the doping concentration. (See Fig. 7.)

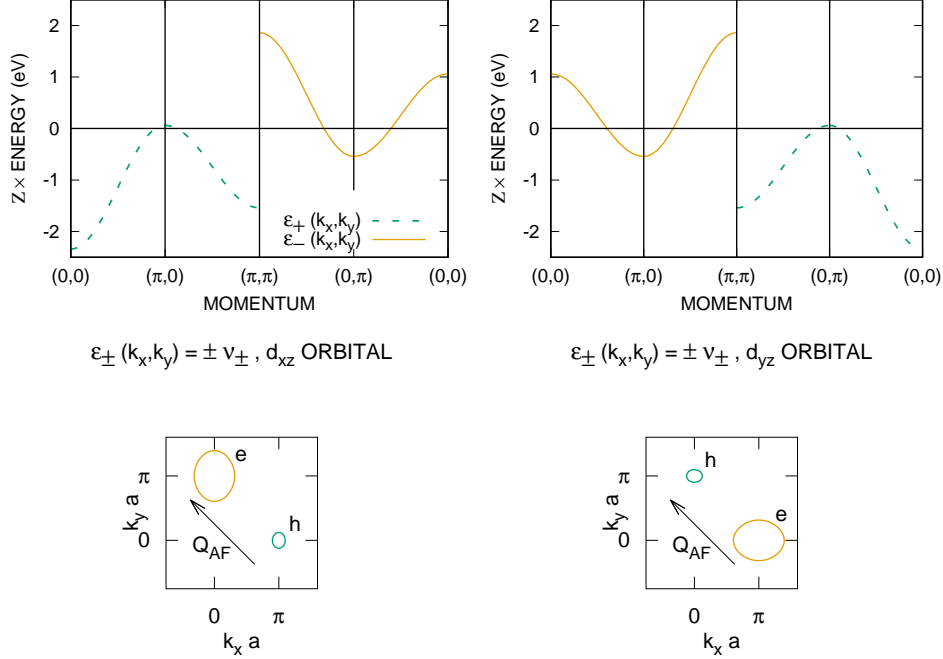


FIG. 6: Renormalized electron bands and Fermi surfaces at electron doping after the Lifshitz transition. Again, the orbital character is only approximate.

### C. Moderate Electron Doping

Let us next seek solutions to the Eliashberg equations, (36a-36c), at moderate electron doping  $x \sim x_0$ . The previous linear response due to weak electron doping predicts a rigid shift in energy of the renormalized electronic structure at half filling displayed by Fig. 5. It is depicted by Fig. 6, where the top of the bonding (+) band lies just above the Fermi level. The previous linear response about half filling also predicts wavefunction renormalizations  $Z_2$  and  $Z_1$  for the bonding band ( $n = 2$ ) and for the anti-bonding band ( $n = 1$ ), respectively, above and below the unique value at half filling. What then does the third Eliashberg equation for the superconducting gap (36c) predict at moderate doping?

We shall follow the historical approach for the solution of the Eliashberg equations in the case of the electron-phonon interaction<sup>41,42,49–52</sup>. In particular, before confronting the gap equation, it is useful first to obtain the wavefunction renormalizations of the two bands at the Fermi level in the normal state. Neglecting frequency dependence, the first Eliashberg equation (36a) then yields the following wavefunction renormalizations at the Fermi level,

$\omega = 0$ :

$$Z_n - 1 = \int_{\Delta_b}^{\omega_{uv}} d\Omega U^2 F_0^{(n, \bar{n})}(\Omega, \mu_n, \mu_{\bar{n}}) \left( \frac{1}{\Omega} - \frac{1}{W/Z_{\bar{n}} + \Omega} \right). \quad (66)$$

Again, the order of integration in (36a) has been reversed. Next, assume weak to moderate wavefunction renormalization in the anti-bonding ( $-$ ) band and strong wavefunction renormalization in the bonding ( $+$ ) band:  $\lambda_1$  such that  $W/Z_1 \gg \Delta_b$ , and  $\lambda_2 \gg 1$  such that  $W/Z_2 \ll \Delta_b$ . Here  $\lambda_n = Z_n - 1$ . Notice that the last inequality is consistent with the previous results at weak electron doping:  $\varepsilon_E/\Delta_b < Z_2$ . The above Eliashberg equations (66) then yield the results

$$\lambda_2 \cong \int_{\Delta_b}^{\omega_{uv}} d\Omega \Omega^{-1} U^2 F_0^{(2,1)}(\Omega, \mu_2, \mu_1), \quad (67)$$

and

$$\lambda_1 \cong \frac{W}{Z_2} \int_{\Delta_b}^{\omega_{uv}} d\Omega \Omega^{-2} U^2 F_0^{(1,2)}(\Omega, \mu_1, \mu_2), \quad (68)$$

or  $\lambda_1 \cong (W/Z_2)\lambda_2 \overline{\Omega^{-1}}$ . The distribution in the average  $\overline{\Omega^{-1}}$  is normalized by the integral (67) because of the approximate identity  $U^2 F_0^{(1,2)}(\Omega, \mu_1, \mu_2) \cong U^2 F_0^{(2,1)}(\Omega, \mu_2, \mu_1)$ . By (37), the latter is due to the approximate identity obeyed by the density of states,  $D_-(\mu_1) \cong D_+(\mu_2)$ , at  $\mu_1$  and  $\mu_2$  near the bottom and near the top of the respective bands  $\varepsilon_-(\mathbf{k})$  and  $\varepsilon_+(\mathbf{k})$ . Here, also, we have applied the identity (51). Because  $\lambda_2 \gg 1$ , we then have that  $\lambda_1 \cong W \overline{\Omega^{-1}}$ . Finally, the initial assumption of moderate  $\lambda_1$  is confirmed by noting that  $W/Z_1 \cong W/(1 + W \overline{\Omega^{-1}}) \cong (\overline{\Omega^{-1}})^{-1}$ , which is much greater than  $\Delta_b$ .

We shall now show that an instability to  $S$ -wave Cooper pairing exists that alternates in sign between the strong electron-type Fermi surface of the anti-bonding ( $-$ ) band,  $n = 1$ , and the weak hole-type Fermi surface of the bonding ( $+$ ) band,  $n = 2$ . (See Fig. 6.) In particular, assume the simple BCS form (47) for the frequency dependence of the respective gaps,  $\Delta_1(\omega)$  and  $\Delta_2(\omega)$ , with frequency cutoffs  $\omega_c(1)$  and  $\omega_c(2)$ . After neglecting the frequency dependence of the wavefunction renormalizations, the gap equations (36c) then read

$$Z_n \Delta_n = -2 \int_{|\Delta_{\bar{n}}|}^{\omega_c(\bar{n})} dE' \frac{\Delta_{\bar{n}}}{\sqrt{E'^2 - \Delta_{\bar{n}}^2}} \int_{\Delta_b}^{\omega_{uv}} d\Omega U^2 F_0^{(n, \bar{n})}(\Omega; \mu_n, \mu_{\bar{n}}) \frac{1}{\Omega + E'}. \quad (69)$$

Assume, further, the BCS limit:  $\omega_c(1), \omega_c(2) \rightarrow 0$ . Taking the normal-state values for the wavefunction renormalizations discussed above is then valid. Also, the denominator above,  $\Omega + E'$ , can then be replaced by  $\Omega$ . After comparison with (67), we thereby arrive at the

gap equations

$$Z_n \Delta_n = -2 \int_{|\Delta_n|}^{\omega_c(\bar{n})} dE' \frac{\lambda_2}{\sqrt{E'^2 - \Delta_n^2}} \Delta_{\bar{n}}, \quad (70)$$

or  $\Delta_1 = -K_{1,2} \Delta_2$  and  $\Delta_2 = -K_{2,1} \Delta_1$ , with kernels

$$K_{1,2} = 2 \frac{\lambda_2}{Z_1} \sinh^{-1} \left[ \frac{\sqrt{\omega_c^2(2) - \Delta_2^2}}{|\Delta_2|} \right] \quad \text{and}$$

$$K_{2,1} = 2 \frac{\lambda_2}{Z_2} \sinh^{-1} \left[ \frac{\sqrt{\omega_c^2(1) - \Delta_1^2}}{|\Delta_1|} \right]. \quad (71)$$

Importantly, these equations imply that  $\Delta_1$  and  $\Delta_2$  are of opposite sign! An  $S^{+-}$  pairing instability therefore exists between the strong and the weak Fermi surfaces shown in Fig. 6.

To obtain explicit solutions of the gap equations, it is useful to multiply and divide these, which yields

$$1 = K_{1,2} K_{2,1} \quad \text{and} \quad \left( \frac{\Delta_2}{\Delta_1} \right)^2 = \frac{K_{2,1}}{K_{1,2}}. \quad (72)$$

Taking the product of the above then gives  $|\Delta_2/\Delta_1| = K_{2,1} \cong 2 \sinh^{-1}[\sqrt{\omega_c^2(1) - \Delta_1^2}/|\Delta_1|]$ . Assuming  $|\Delta_1|$  near  $\omega_c(1)$  in turn yields  $|\Delta_2| \cong 2\sqrt{2\omega_c(1)}\sqrt{\omega_c(1) - |\Delta_1|}$ . Substituting the previous into the first gap equation displayed by (72) then yields

$$1 \cong 2 \frac{\lambda_2}{Z_1 \omega_c(1)} \sinh^{-1} \left[ \frac{\omega_c(2)}{|\Delta_2|} \right], \quad (73)$$

or  $|\Delta_2| \sim (Z_1/Z_2)|\Delta_1|$ , with  $|\Delta_1| \cong \omega_c(1)$ . This solution thereby confirms the instability of the Fermi surfaces to  $S^{+-}$  pairing, where the wavefunction renormalization  $Z_1$  on the larger electron-type Fermi surface is of moderate size compared to unity, while the wavefunction renormalization  $Z_2$  on the smaller hole-type Fermi surface is large compared to unity. (See Fig. 6.)

## V. DISCUSSION

The previous results of electron Fermi surface pockets and faint hole Fermi surface pockets at the corner of the folded (two-iron) Brillouin zone, with  $S^{+-}$  Cooper pairing that alternates in sign between them, is compared below to a local-moment model for electron-doped iron selenide and to high-temperature iron-selenide superconductors themselves.



### A. Comparison with Local-Moment Model

A local-moment model of the electronic physics in electron-doped iron selenide exists that captures many of the principal features of the above Eliashberg theory<sup>29</sup>. It emerges near half filling in the strong correlation limit,  $U_0 \rightarrow \infty$ . By (13), isospin symmetry is broken strongly along the  $I^{(3)}$  axis in such a case. In particular, doubly occupied orbital states listed in Table I are projected out. The following Hund-Heisenberg model in terms of the spin operators  $\mathbf{S}_{i,d+}$  and  $\mathbf{S}_{i,d-}$  then accurately describes the spin dynamics<sup>34</sup>:

$$H_{\text{HH}} = \sum_i J_0 \mathbf{S}_{i,d-} \cdot \mathbf{S}_{i,d+} + \sum_{\langle i,j \rangle} (J_1^{\parallel} \mathbf{S}_{i,\alpha} \cdot \mathbf{S}_{j,\alpha} + J_1^{\perp} \mathbf{S}_{i,\alpha} \cdot \mathbf{S}_{j,\bar{\alpha}}) \\ + \sum_{\langle\langle i,j \rangle\rangle} (J_2^{\parallel} \mathbf{S}_{i,\alpha} \cdot \mathbf{S}_{j,\alpha} + J_2^{\perp} \mathbf{S}_{i,\alpha} \cdot \mathbf{S}_{j,\bar{\alpha}}). \quad (74)$$

Here the index  $\alpha$  is implicitly summed over the iron  $d+$  and  $d-$  orbitals. The intra-orbital ( $\parallel$ ) and inter-orbital ( $\perp$ ) Heisenberg exchange coupling constants are positive, and they satisfy  $J_1^{\parallel} > J_1^{\perp}$  and  $J_2^{\parallel} = J_2^{\perp}$ . The above spin Hamiltonian also contains Hund's Rule exchange coupling between the orbitals, with a ferromagnetic coupling constant,  $J_0 < 0$ . Again, the infinite- $U_0$  limit is taken, which means that the formation of spin singlets per site, per  $d+$  or  $d-$  orbital, is suppressed. Electron hopping via the Hamiltonian  $H_{\text{hop}}$  (1) is also added at electron doping, but in the infinite- $U_0$  limit. Last, notice that orbital swap,  $d- \leftrightarrow d+$ , is a global symmetry of the Hund-Heisenberg Hamiltonian (74). It is therefore most natural to consider the case where orbital swap  $P_{d,\bar{d}}$  is a global symmetry of the hopping Hamiltonian  $H_{\text{hop}}$  (1) as well. This requires the absence of mixing between the  $3d_{xz}$  and  $3d_{yz}$  orbitals:  $t_2^{\perp} = 0$ . The latter restriction for the validity of the two-orbital  $t$ - $J$  model emerges from the underlying extended Hubbard model in the large- $U_0$  limit at half filling<sup>26</sup>. In such case, for example, the transverse spin susceptibilities of both models,  $\chi_{\perp}$ , coincide only in the limit  $t_2^{\perp}/i \rightarrow 0$ .

The author exploited the Schwinger-boson-slave-fermion representation of the correlated electron to study the above local-moment model<sup>29</sup>. Here, the correlated electron *fractionalizes* into a Schwinger boson that carries spin and a slave fermion that carries charge. At half filling, an hSDW of the type depicted by Fig. 3b is predicted at  $J_1^{\parallel} > J_1^{\perp}$  and at Hund's Rule exchange coupling<sup>29,34</sup>,  $-J_0$ , below a critical one. In particular, a quantum-critical point exists at moderate Hund's Rule coupling  $-J_{0c}$ , where the spin-excitation spectrum collapses to zero energy at stripe SDW wave numbers  $(\pi/a, 0)$  and  $(0, \pi/a)$ . Specifically, the

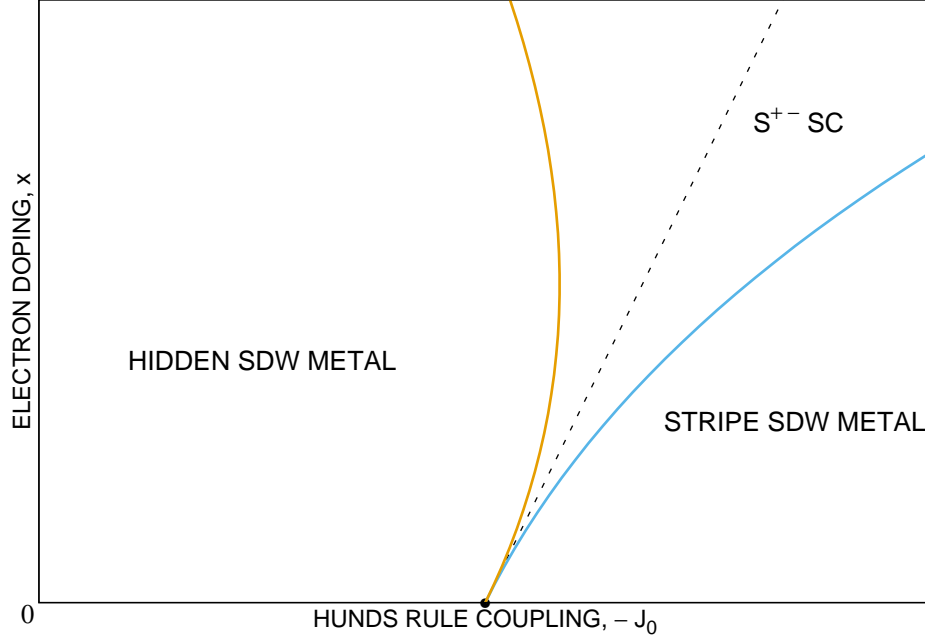


FIG. 7: Proposed phase diagram for local-moment model of electron-doped iron selenide (ref.<sup>29</sup>). The latter predicts the phase boundary approaching half filling (dashed line), which separates the hSDW state from the stripe SDW state. The intervening  $S^{+-}$  superconducting phase is predicted by the Eliashberg Theory introduced in the main text.

QCP occurs at<sup>29,34</sup>

$$-J_{0c} = 2(J_1^{\parallel} - J_1^{\perp}) + 2t_1^{\perp}x/(1-x)^2s_0 - 4J_2^{\parallel} \quad (75)$$

in the minimal case where only the  $t_1^{\perp}(\hat{x}) = -t_1^{\perp}(\hat{y})$  hopping matrix elements are non-zero. Here,  $x$  denotes the concentration of electron doping from half filling, while  $s_0$  denotes the spin of the electron. The quantum-critical line (75) is depicted by the dashed line in Fig. 7. It is possible to identify the critical normal state of the previous Eliashberg theory at half filling ( $\Delta_b, \Delta_1, \text{ and } \Delta_2 \rightarrow 0$ ) with this QCP.

Both Schwinger-boson-slave-fermion mean field theory about the hidden Néel state and exact calculations on finite clusters for the above local-moment model find evidence for a  $d_{xz}$  and a  $d_{yz}$  Fermi-surface pocket at the corner of the two-iron Brillouin zone, at electron doping<sup>29</sup>. This result agrees with the previous results based on Eliashberg Theory, which are summarized by Fig. 6. Yet how does the area of the slave-fermion Fermi-surface pockets compare with that predicted by the previous Eliashberg theory, Fig. 6? Because the slave

fermions do not carry spin, we have by charge conservation that

$$[D_+(\text{top}) + D_-(\text{bottom})]\delta\mu = 2[D_+(0) + D_-(0)]\mu_0. \quad (76)$$

The left-hand and the right-hand sides above correspond, respectively, to the cases where interactions are turned on (Fig. 5) and turned off (Fig. 1). In the above Eliashberg theory, (36a)-(36c) and (37), it has been assumed throughout that  $D_+(\varepsilon) \cong D_+(\text{top})$  and that  $D_-(\varepsilon) \cong D_-(\text{bottom})$ , however. Within that approximation, (76) thereby yields the susceptibility

$$\chi_E = \frac{\delta\mu}{\mu_0} \cong 2$$

from the Schwinger-boson-slave-fermion mean field theory. It agrees with the corresponding result from Eliashberg theory listed in Table VI, at hopping matrix element  $t_1^\parallel \rightarrow 0$ , in which case the renormalized Fermi-surface pockets become perfectly circular as  $U_0$  grows large ( $x_0 \rightarrow 0$ ). This coincides with the hopping parameters studied in the local-moment model within the mean-field approximation<sup>29</sup>, in which case only  $t_1^\perp$  is non-zero.

And how do the predictions for wavefunction renormalization by the previous Eliashberg theory compare with the local-moment model<sup>29</sup>? A faint hole band with quasi-particle weight  $1/Z_2$  that vanishes at criticality,  $\Delta_b \rightarrow 0$ , is predicted by Eliashberg theory. (See Fig. 6.) It crosses the Fermi level near the corner of the folded (two-iron) Brillouin zone. At electron doping, both mean field theory and exact calculations on finite clusters find *no* evidence for low-energy hole excitations in the two-orbital  $t$ - $J$  model at momenta  $(\pi/a, 0)$  and  $(0, \pi/a)$ . This is consistent with the previous. Also, in the limit of large electron spin  $s_0$ , Schwinger-boson-slave-fermion mean field theory yields a coherent contribution to the one-particle Greens function equal to  $G_{\text{coh}}(\mathbf{k}, \omega) = s_0/[\omega + \mu_1 - \varepsilon_-(\mathbf{k})]$ . This is also consistent with the appreciable quasi-particle weight  $1/Z_1$  predicted by Eliashberg theory at electron doping for the electron-type Fermi surface pockets at the corner of the two-iron Brillouin zone.

Last, exact calculations of the local-moment model for electron-doped FeSe on finite clusters find evidence for an  $S$ -wave Cooper pair at an energy below a continuum of states near the QCP<sup>29</sup>. This is consistent with the prediction made above by Eliashberg theory for an instability of the Fermi surface to  $S^{+-}$  superconductivity. The former exact calculations also find a  $D$ -wave Cooper pair at an energy below the continuum of states, but lying above

the  $S$ -wave Cooper pair. The separation in energy between the two pair states collapses to zero at the QCP.

Finally, the Schwinger-boson-slave-fermion mean field theory for the local-moment model assumes only inter-orbital nearest neighbor hopping between iron atoms<sup>29</sup>,  $t_1^\perp(\hat{\mathbf{x}}) = -t_1^\perp(\hat{\mathbf{y}})$ . Such hopping of electrons leaves the two sublattices of the hidden Néel order displayed by Fig. 3b intact. Yet intra-orbital hopping of electrons across next-nearest neighbors,  $t_2^\parallel$ , also leaves the sublattices for hidden Néel order intact. Switching it on then leaves the predictions for the local-moment model mentioned above<sup>29</sup> unchanged. Direct calculation of the Schwinger-boson-slave-fermion mean field theory confirms this claim for  $|t_1^\perp| > 2t_2^\parallel$ . Because the results of the local-moment model coincide with those of the Eliashberg Theory for the extended Hubbard model obtained in the previous section, we believe that the latter can remain valid off perfect nesting (7), at  $t_2^\parallel \neq 0$ .

## B. Comparison with Experiment

The prediction displayed by Fig. 6 of electron-type Fermi surface pockets centered at the corner of the two-iron Brillouin zone agrees with ARPES on electron-doped iron selenide<sup>1,9,14</sup>. Eliashberg theory also predicts the opening of an  $S$ -wave gap over such Fermi surface pockets, which also agrees with ARPES on these systems<sup>2,10,11,13</sup>, as well as with STM<sup>5,12,15</sup>. Electron-electron interactions are expected to be moderately strong in iron selenide. This rules out conventional  $S$ -wave pairing over the electron Fermi surface pockets in electron-doped iron selenide. The  $S^{+-}$  Cooper pairing that is predicted here between the electron Fermi surface pockets and faint hole Fermi surface pockets at the corner of the folded Brillouin zone therefore potentially resolves the puzzling observations of isotropic pair gaps in electron-doped iron selenide. In particular, the frequency cutoff for the hidden spin fluctuations that appears in the gap equations (71)-(73) obtained from Eliashberg Theory is approximately  $\omega_c(1) \cong 2k_{F1}c_b = 2(2\pi x_1)^{1/2}c_b/a$  in the case of the anti-bonding band,  $n = 1$ , where  $x_1$  denotes the concentration of each electron pocket. The Hund-Heisenberg model (74) at half filling predicts a hidden-spin-wave velocity in the hSDW state of<sup>34</sup>

$$c_b/a = 2s_1 \left[ \left( J_1^\parallel - J_1^\perp \right) \left( \frac{1}{2}J_0 + 2J_1^\parallel + 2J_2^\perp \right) \right]^{1/2}, \quad (77)$$

at  $J_2^{\parallel} = J_2^{\perp}$ . ARPES on electron-doped iron selenide finds a gap in the range  $\Delta_1 = 10\text{-}20$  meV at zero temperature<sup>2,10,11,13</sup>. Let us set  $J_1^{\perp} = 0$  and assume values for the remaining Heisenberg exchange coupling constants and the Hund's Rule exchange coupling constant of order<sup>34</sup>  $|J_0|, J_1^{\parallel}, J_2^{\parallel} = J_2^{\perp} \sim 100$  meV. At moderately small electron pockets,  $2(2\pi x_1)^{1/2} \sim 1$ , this then yields a gap  $\Delta_1 \cong \omega_c(1)$  that is of order the gap determined by ARPES for low ordered moments,  $s_1 < 1/2$ .

The spectrum of hidden spin fluctuations centered at the antiferromagnetic wave number  $\mathbf{Q}_{\text{AF}} = (\pi/a, \pi/a)$  is what binds together electrons into  $S^{+-}$  Cooper pairs in the present Eliashberg theory. Recent inelastic neutron scattering studies on intercalated iron selenide<sup>53</sup> find low-energy magnetic excitations at wave numbers *around*  $\mathbf{Q}_{\text{AF}}$ , but no low-energy spin excitations *at*  $\mathbf{Q}_{\text{AF}}$ . Such a ring of low-energy magnetic excitations is in fact consistent with the low-energy hidden spin fluctuations that are exploited by the present Eliashberg theory. In particular, both the two-orbital local-moment model discussed above and the underlying extended Hubbard model for electron-doped iron selenide described in subsection II B predict that the low-energy hidden spin fluctuations centered at  $\mathbf{Q}_{\text{AF}}$  are not observable in the true-spin channel of the iron atoms<sup>26,38</sup>. This leaves a ring of observable spin excitations around the antiferromagnetic wavevector  $\mathbf{Q}_{\text{AF}}$ , in agreement with inelastic neutron scattering<sup>53</sup>.

### C. Iron $3d_{xy}$ Orbital, Buried Hole Bands, and Polarization Correction

Although the present study suggests that the iron  $3d_{xz}/3d_{yz}$  orbitals are the principal ones in electron-doped iron selenide, ARPES and density-functional theory indicate that the iron  $3d_{xy}$  orbital also plays an important role<sup>54</sup>. Indeed, it is quite possible that the two  $3d_{xz}/3d_{yz}$  bands and the  $3d_{xy}$  band are approximately half filled in electron-doped iron selenide<sup>21,55</sup>. Doubly occupied  $3d_{x^2-y^2}$  and  $3d_{x^2+y^2-2z^2}$  orbitals are consistent with such fillings among the iron  $3d$  bands. Electron doping could achieve an atomic configuration  $[\text{Ar}]3d^74s^2$  for  $\text{Fe}^-$ , which in turn is consistent with such occupancies among the  $3d$  orbitals. A relatively flat and hole-type  $3d_{xy}$  band can be added to the present Eliashberg Theory for  $3d_{xz}/3d_{yz}$  electrons interacting with hidden spin fluctuations (Fig. 4). (See ref.<sup>56</sup>, Fig. S1.) Because electrons in the  $3d_{xy}$  band do *not* interact with hidden spin fluctuations, they may be considered to be spectators. Weak mixing of the two  $3d_{xz}/3d_{yz}$  bands with the  $3d_{xy}$  band results in the expected level repulsion of the renormalized electron/hole Fermi surface

pockets shown in Fig. 5. (See ref.<sup>56</sup>, Fig. S3.) This implies that the Lifshitz transition to such a renormalized band structure at half filling is robust in the presence of weak mixing with the  $3d_{xy}$  band. Also, within the present Eliashberg Theory, a direct calculation of the propagator for such  $3d_{xy}$  spectator electrons finds that they inherit divergent wavefunction renormalization at the Fermi level from the  $3d_{xz}/3d_{yz}$  electrons at half filling. (See ref.<sup>56</sup>, Eq. (S20).) In particular, the vanishing quasi-particle weight of the  $3d_{xz}/3d_{yz}$  electrons at the Fermi level,  $Z^{-1} \rightarrow 0$ , implies the vanishing quasi-particle weight of the  $3d_{xy}$  electrons at the Fermi level. (Cf. ref.<sup>55</sup>.) Similar results are obtained when the spin-orbit interaction is included on iron atoms that are strictly equivalent over the square lattice<sup>56</sup>. Last, the tips of the electron Fermi surface pockets ( $n = 1$ ) shown in Fig. 5 can acquire  $3d_{xy}$  orbital character if the electron/hole Fermi surface pockets are large enough. This coincides with predictions made by band-structure calculations on alkali-atom intercalated iron selenides<sup>18,20</sup>.

ARPES on electron-doped iron selenide finds hole-type bands at the center of the unfolded Brillouin zone that lie below the bottom of the electron-type bands at the corner of the folded Brillouin zone<sup>1,9,11,13,14</sup>. Schwinger-boson-slave-fermion mean field theory of the local-moment model mentioned previously finds evidence for incoherent hole bands buried below the Fermi level at the  $\Gamma$ -point as well<sup>29</sup>. The present calculations based on Eliashberg theory do not predict such hole-type bands, however. Figure 1 shows bare bonding and anti-bonding bands near the Fermi level that become degenerate at momenta  $\mathbf{k} = (0, 0)$  and  $(\pi/a, \pi/a)$  in the unfolded Brillouin zone. The two bands show opposite curvatures at these points when the hybridization between the  $3d_{xz}$  and  $3d_{yz}$  orbitals lies inside the window  $t_1^{\parallel} < 2|t_2^{\perp}| < |t_1^{\perp}|$ . It is possible that including momentum and/or frequency dependence in the present Eliashberg Theory opens a gap at the Fermi level at these  $\Gamma$ -points in momentum space. Such a calculation lies outside the scope of the present one, however.

Absent from the previous calculations of the electron self-energy corrections within Eliashberg Theory, Fig. 4, is the polarization correction<sup>41,42</sup> to the propagator (15) for hidden spinwaves. Recall the wavefunction renormalization for electrons near the Fermi surface at half filling:  $Z = \varepsilon_E/\Delta_b$ . The former polarization correction therefore *vanishes* at the QCP, where  $\Delta_b \rightarrow 0$ . Proximity to the QCP is assumed throughout, which justifies the neglect of the polarization correction to the propagation of hidden spinwaves.

## VI. CONCLUSIONS

We have shown above how low-energy hidden spin fluctuations near the wavevector for the checkerboard on the square lattice of iron atoms in electron-doped iron selenide lead to superconductivity, with isotropic Cooper pairs that alternate in sign between strong electron Fermi surface pockets and faint hole Fermi surface pockets. (See Fig. 6.) By contrast with the incipient-band mechanism for  $S^{+-}$  superconductivity<sup>48</sup>, the latter do *not* coincide with the hole bands buried below the Fermi level at the center of the Brillouin zone. Both electron and hole Fermi surface pockets lie at the corner of the folded (two-iron) Brillouin zone. A comparison of the gap that is predicted to open over the electron Fermi surface pockets with that observed by ARPES<sup>2,10,11,13</sup> is consistent with short-range hidden magnetic order, with a moderate to weak ordered moment.

Like true spin fluctuations in the case of iron-pnictide materials<sup>45–47</sup>, the hidden spin fluctuations studied here are due to nested Fermi surfaces. In the present case, however, the exchange of hidden spin fluctuations give rise to significant band shifts. In particular, Eliashberg theory reveals that they incite a Lifshitz transition from nested Fermi surfaces at the center and at the corner of the unfolded (one-iron) Brillouin zone to nested Fermi surfaces at the corner of the folded Brillouin zone<sup>26</sup>. Also, like true spin fluctuations in the case of iron-pnictide materials<sup>45–47,57–59</sup>, hidden spin fluctuations give rise to repulsive inter-band interactions between electrons that favor  $S^{+-}$  Cooper pairing between the renormalized Fermi surface pockets. In the present case, however, orbital matrix elements result in weak effective inter-band interactions. This justifies the neglect of vertex corrections in Eliashberg theory<sup>41,42</sup>.

It has also been recently argued by the author that hidden spin fluctuations account for the ring of low-energy spin excitations at the checkerboard wavevector observed by inelastic neutron scattering in electron-doped iron selenide<sup>38,53</sup>. This, coupled with the prediction of  $S^{+-}$  superconductivity described above, suggests that hidden spin fluctuations play an important role in high-temperature iron-selenide superconductors.

## **Acknowledgments**

The author is indebted to Stefan-Ludwig Drechsler for suggesting Eliashberg Theory in both the particle-hole and in the particle-particle channels. (Cf. ref.<sup>51</sup>, Chapter 5.) He also thanks Yongtao Cui for useful discussions, and he acknowledges the hospitality of the Kavli Institute for Theoretical Physics. This work was supported in part by the US Air Force Office of Scientific Research under grant No. FA9550-17-1-0312 and by the National Science Foundation under Grant No. NSF PHY-1748958.



## Appendix A: Spin and Isospin Operators

The spin operator at iron site  $i$  and orbital  $\alpha$  is the usual contraction of Pauli matrices  $\boldsymbol{\sigma}$  over spin quantum numbers:

$$\mathbf{S}_{i,\alpha} = \frac{\hbar}{2} \sum_{s=\uparrow,\downarrow} \sum_{s'=\uparrow,\downarrow} c_{i,\alpha,s}^\dagger \boldsymbol{\sigma}_{s,s'} c_{i,\alpha,s'}. \quad (\text{A1})$$

The spin operator at iron site  $i$  is then

$$\mathbf{S}_i = \mathbf{S}_{i,d+} + \mathbf{S}_{i,d-}. \quad (\text{A2})$$

The isospin operator at iron site  $i$  and for spin  $s$ , on the other hand, is the contraction of Pauli matrices  $\boldsymbol{\tau}$  over the two orbital quantum numbers:

$$\mathbf{I}_{i,s} = \frac{1}{2} \sum_{\alpha=d+,d-} \sum_{\alpha'=d+,d-} c_{i,\alpha,s}^\dagger \boldsymbol{\tau}_{\alpha,\alpha'} c_{i,\alpha',s}. \quad (\text{A3})$$

The isospin operator at iron site  $i$  is then

$$\mathbf{I}_i = \mathbf{I}_{i,\uparrow} + \mathbf{I}_{i,\downarrow}. \quad (\text{A4})$$

Last, the operator for the tensor product of the spin with isospin is the contraction of  $\boldsymbol{\sigma}\boldsymbol{\tau}$  over both the spin and isospin quantum numbers:

$$(\mathbf{S} \otimes \mathbf{I})_i = \frac{\hbar}{4} \sum_{s=\uparrow,\downarrow} \sum_{\alpha=d+,d-} \sum_{\alpha'=d+,d-} \sum_{s'=\uparrow,\downarrow} c_{i,\alpha,s}^\dagger \boldsymbol{\sigma}_{s,s'} \boldsymbol{\tau}_{\alpha,\alpha'} c_{i,\alpha',s'}. \quad (\text{A5})$$

## Appendix B: Orbital Matrix Element

The operators that create the eigenstates (5) of the electron hopping Hamiltonian,  $H_{\text{hop}}$ , are

$$c_s^\dagger(n, \mathbf{k}) = \mathcal{N}^{-1/2} \sum_i \sum_{\alpha=0,1} (-1)^{\alpha n} e^{i(2\alpha-1)\delta(\mathbf{k})} e^{i\mathbf{k}\cdot\mathbf{r}_i} c_{i,\alpha,s}^\dagger, \quad (\text{B1})$$

where  $\alpha = 0$  and  $1$  index the  $d-$  and  $d+$  orbitals, and where  $n = 1$  and  $2$  index the anti-bonding and bonding orbitals  $(-i)d_{y(\delta)z}$  and  $d_{x(\delta)z}$ . The inverse of the above is then

$$c_{i,\alpha,s}^\dagger = \mathcal{N}^{-1/2} \sum_{\mathbf{k}} \sum_{n=1,2} (-1)^{\alpha n} e^{-i(2\alpha-1)\delta(\mathbf{k})} e^{-i\mathbf{k}\cdot\mathbf{r}_i} c_s^\dagger(n, \mathbf{k}). \quad (\text{B2})$$

Plugging (B2) and its hermitian conjugate into the expression for the hidden electron spin operator,

$$\mathbf{S}(\pi, \mathbf{q}) = \frac{1}{2} \sum_s \sum_{s'} \sum_i \sum_\alpha (-1)^\alpha e^{i\mathbf{q}\cdot\mathbf{r}_i} \frac{1}{2} c_{i,\alpha,s}^\dagger \boldsymbol{\sigma}_{s,s'} c_{i,\alpha,s'}, \quad (\text{B3})$$

yields the form

$$\mathbf{S}(\pi, \mathbf{q}) = \frac{1}{2} \sum_s \sum_{s'} \sum_{\mathbf{k}} \sum_{n,n'} \mathcal{M}_{n,\mathbf{k};n',\mathbf{k}'} c_s^\dagger(n', \mathbf{k}') \boldsymbol{\sigma}_{s,s'} c_{s'}(n, \mathbf{k}), \quad (\text{B4})$$

with the matrix element<sup>26</sup>

$$\mathcal{M}_{n,\mathbf{k};n',\mathbf{k}'} = \begin{cases} -i \sin[\delta(\mathbf{k}) - \delta(\mathbf{k}')] & \text{for } n' = n, \\ \cos[\delta(\mathbf{k}) - \delta(\mathbf{k}')] & \text{for } n' \neq n. \end{cases} \quad (\text{B5})$$

Here,  $\mathbf{k}' = \mathbf{k} - \mathbf{q}$ . Now replace  $\mathbf{k}'$  above with  $\bar{\mathbf{k}}' = \mathbf{k}' + \mathbf{Q}_{\text{AF}}$ . Using the identity

$$\delta(\mathbf{k}' + \mathbf{Q}_{\text{AF}}) = \pm \frac{\pi}{2} - \delta(\mathbf{k}') \quad (\text{B6})$$

yields the equivalent expression<sup>26</sup>

$$\mathcal{M}_{n,\mathbf{k};n',\bar{\mathbf{k}}'} = \begin{cases} \pm i \cos[\delta(\mathbf{k}) + \delta(\mathbf{k}')] & \text{for } n' = n, \\ \pm \sin[\delta(\mathbf{k}) + \delta(\mathbf{k}')] & \text{for } n' \neq n. \end{cases} \quad (\text{B7})$$

Here,  $\mathbf{k}' = \mathbf{k} - \mathbf{q} - \mathbf{Q}_{\text{AF}}$ .

### Appendix C: Definite Integrals Approaching Criticality

The following definite integrals appear in the solution of the Eliashberg equations (43) at half filling, at criticality:

$$I(y) = \int_0^\infty dx \frac{1}{y + \cosh x}, \quad (\text{C1})$$

and

$$J(y) = \int_0^\infty dx \ln \left( 1 + \frac{y}{\cosh x} \right). \quad (\text{C2})$$

The first one (C1) can be evaluated directly by using the definition  $\cosh x = \frac{1}{2}z + \frac{1}{2}z^{-1}$ , with  $z = e^x$ . Changing variables leads to the expression

$$I(y) = \int_1^\infty dz \frac{2}{z^2 + 2yz + 1}. \quad (\text{C3})$$

Factorizing the denominator into  $(z - z_+)(z - z_-)$ , with  $z_{\pm} = -y \pm \sqrt{y^2 - 1}$ , and resolving the integrand into partial fractions yields

$$I(y) = \int_1^{\infty} dz \frac{1}{z_+ - z_-} \left( \frac{1}{z - z_+} - \frac{1}{z - z_-} \right). \quad (\text{C4})$$

Hence, we arrive at the closed-form expression

$$I(y) = \frac{1}{\sqrt{y^2 - 1}} \ln \left( \frac{1 + y + \sqrt{y^2 - 1}}{1 + y - \sqrt{y^2 - 1}} \right). \quad (\text{C5})$$

Simplifying the argument of the logarithm above yields the equivalent expression

$$I(y) = \frac{1}{\sqrt{y^2 - 1}} \ln \left( \frac{1}{y - \sqrt{y^2 - 1}} \right). \quad (\text{C6})$$

And concerning the second definite integral (C2), notice that (i)  $dJ/dy = I$  and (ii)  $J(0) = 0$ .

The expression

$$J(y) = \frac{\pi^2}{8} + \frac{1}{2} [\ln(y - \sqrt{y^2 - 1})]^2 \quad (\text{C7})$$

satisfies both conditions. It therefore coincides with the definite integral (C2).

Further, the constant  $F$  that appears in the linear response at half filling to electron doping can also be evaluated in closed form. Expression (62) for it can be re-expressed as

$$F = \lim_{\Delta_b \rightarrow 0} \frac{1}{2} \frac{\epsilon_E}{\Delta_b} \left[ \int_0^{x_2} dx \operatorname{sech} x + \frac{\partial}{\partial y} \int_0^{x_2} dx (1 + y \operatorname{sech} x)^{-1} \right], \quad (\text{C8})$$

where  $x_2 = \cosh^{-1}(\omega_{uv}/\Delta_b)$ . But  $(1 + y \operatorname{sech} x)^{-1} = 1 - y(y + \cosh x)^{-1}$ , which yields the identity

$$\int_0^{x_2} dx (1 + y \operatorname{sech} x)^{-1} = x_2 - y \int_0^{x_2} dx (y + \cosh x)^{-1}.$$

Substituting it above then yields the closed-form expression

$$F = \frac{1}{2} \frac{\epsilon_E}{\Delta_b} \left[ \frac{\pi}{2} - I(y) - yI'(y) \right] \quad (\text{C9})$$

as  $\Delta_b \rightarrow 0$ , where  $I'(y)$  is the derivative of (C6).

- 
- <sup>1</sup> T. Qian, X.-P. Wang, W.-C. Jin, P. Zhang, P. Richard, G. Xu, X. Dai, Z. Fang, J.-G. Guo, X.-L. Chen, H. Ding, “Absence of a Holelike Fermi Surface for the Iron-Based  $K_{0.8}Fe_{1.7}Se_2$  Superconductor Revealed by Angle-Resolved Photoemission Spectroscopy”, *Phys. Rev. Lett.* **106**, 187001 (2011).
- <sup>2</sup> M. Xu, Q. Q. Ge, R. Peng, Z. R. Ye, Juan Jiang, F. Chen, X. P. Shen, B. P. Xie, Y. Zhang, A. F. Wang, X. F. Wang, X. H. Chen, and D. L. Feng, “Evidence for an S-Wave Superconducting Gap in  $K_xFe_{2-y}Se_2$  from Angle-Resolved Photoemission”, *Phys. Rev. B* **85**, 220504(R) (2012).
- <sup>3</sup> B. Zeng, B. Shen, G. F. Chen, J. B. He, D. M. Wang, C. H. Li, and H. H. Wen, “Nodeless Superconductivity of Single-Crystalline  $K_xFe_{2-y}Se_2$  Revealed by the Low-Temperature Specific Heat”, *Phys. Rev. B* **83**, 144511 (2011).
- <sup>4</sup> Weiqiang Yu, L. Ma, J. B. He, D. M. Wang, T.-L. Xia, G. F. Chen, and Wei Bao, “ $^{77}Se$  NMR Study of the Pairing Symmetry and the Spin Dynamics in  $K_yFe_{2-x}Se_2$ ”, *Phys. Rev. Lett.* **106**, 197001 (2011).
- <sup>5</sup> Q.-Y. Wang, Z. Li, W.-H. Zhang, Z.-C. Zhang, J.-S. Zhang, W. Li, H. Ding, Y.-B. Ou, P. Deng, K. Chang, J. Wen, C.-L. Song, K. He, J.-F. Jia, S.-H. Ji, Y. Wang, L. Wang, X. Chen, X. Ma, Q.-K. Xue, “Interface-Induced High-Temperature Superconductivity in Single Unit-Cell FeSe Films on  $SrTiO_3$ ”, *Chin. Phys. Lett.* **29**, 037402 (2012).
- <sup>6</sup> W.-H. Zhang, Y. Sun, J.-S. Zhang, F.-S. Li, M.-H. Guo, Y.-F. Zhao, H.-M. Zhang, J.-P. Peng, Y. Xing, H.-C. Wang, T. Fujita, A. Hirata, Z. Li, H. Ding, C.-J. Tang, M. Wang, Q.-Y. Wang, K. He, S.-H. Ji, X. Chen, J.-F. Wang, Z.-C. Xia, L. Li, Y.-Y. Wang, J. Wang, L.-L. Wang, M.-W. Chen, Q.-K. Xue, and X.-C. Ma, “Direct Observation of High-Temperature Superconductivity in One-Unit-Cell FeSe Films”, *Chin. Phys. Lett.* **31**, 017401 (2014).
- <sup>7</sup> L.Z. Deng, B. Lv, Z. Wu, Y.Y. Xue, W.H. Zhang, F.S. Li, L.L. Wang, X.C. Ma, Q.K. Xue, and C.W. Chu, “Meissner and Mesoscopic Superconducting States in 14 Unit-Cell FeSe Films”, *Phys. Rev. B* **90**, 214513 (2014).
- <sup>8</sup> J.-F. Ge, Z.-L. Liu, C. Liu, C.-L. Gao, D. Qian, Q.-K. Xue, Y. Liu, J.-F. Jia, “Superconductivity Above 100 K in Single-Layer FeSe Films on Doped  $SrTiO_3$ ”, *Nat. Mater.* **14**, 285 (2015).
- <sup>9</sup> D. Liu, W. Zhang, D. Mou, J. He, Y.-B. Ou, Q.-Y. Wang, Z. Li, L. Wang, L. Zhao, S. He, Y. Peng, X. Liu, C. Chaoyu, L. Yu, G. Liu, X. Dong, J. Zhang, C. Chen, Z. Xu, J. Hu, X. Chen,

- Z. Ma, Q. Xue and X.J. Zhou, “Electronic Origin of High-Temperature Superconductivity in Single-Layer FeSe Superconductor”, *Nat. Comm.* **3**, 931 (2012).
- <sup>10</sup> R. Peng, X.P. Shen, X. Xie, H.C. Xu, S.Y. Tan, M. Xia, T. Zhang, H.Y. Cao, X.G. Gong, J.P. Hu, B.P. Xie, D. L. Feng, “Measurement of an Enhanced Superconducting Phase and a Pronounced Anisotropy of the Energy Gap of a Strained FeSe Single Layer in FeSe/Nb: SrTiO<sub>3</sub>/KTaO<sub>3</sub> Heterostructures Using Photoemission Spectroscopy”, *Phys. Rev. Lett.* **112**, 107001 (2014).
- <sup>11</sup> J.J. Lee, F.T. Schmitt, R.G. Moore, S. Johnston, Y.-T. Cui, W. Li, M. Yi, Z.K. Liu, M. Hashimoto, Y. Zhang, D.H. Lu, T.P. Devereaux, D.-H. Lee and Z.-X. Shen, “Interfacial Mode Coupling as the Origin of the Enhancement of  $T_c$  in FeSe Films on SrTiO<sub>3</sub>”, *Nature* **515**, 245 (2014).
- <sup>12</sup> Q. Fan, W.H. Zhang, X. Liu, Y.J. Yan, M.Q. Ren, R. Peng, H.C. Xu, B.P. Xie, J.P. Hu, T. Zhang, and D.L. Feng, “Plain S-Wave Superconductivity in Single-Layer FeSe on SrTiO<sub>3</sub> Probed by Scanning Tunneling Microscopy”, *Nat. Phys.* **11**, 946 (2015).
- <sup>13</sup> L. Zhao, A. Liang, D. Yuan, Y. Hu, D. Liu, J. Huang, S. He, B. Shen, Y. Xu, X. Liu, L. Yu, G. Liu, H. Zhou, Y. Huang, X. Dong, F. Zhou, Z. Zhao, C. Chen, Z. Xu, X.J. Zhou, “Common Electronic Origin of Superconductivity in (Li,Fe)OHFeSe Bulk Superconductor and Single-Layer FeSe/SrTiO<sub>3</sub> Films”, *Nat. Comm.* **7**, 10608 (2016).
- <sup>14</sup> X.H. Niu, R. Peng, H.C. Xu, Y.J. Yan, J. Jiang, D.F. Xu, T.L. Yu, Q. Song, Z.C. Huang, Y.X. Wang, B.P. Xie, X.F. Lu, N.Z. Wang, X.H. Chen, Z. Sun, and D.L. Feng, “Surface Electronic Structure and Isotropic Superconducting Gap in (Li<sub>0.8</sub>Fe<sub>0.2</sub>)OHFeSe”, *Phys. Rev. B* **92**, 060504(R) (2015).
- <sup>15</sup> Y.J. Yan, W.H. Zhang, M.Q. Ren, X. Liu, X.F. Lu, N. Z. Wang, X.H. Niu, Q. Fan, J. Miao, R. Tao, B.P. Xie, X.H. Chen, T. Zhang, D.L. Feng, “Surface Electronic Structure and Evidence of Plain S-Wave Superconductivity in (Li<sub>0.8</sub>Fe<sub>0.2</sub>)OHFeSe”, *Phys. Rev. B* **94**, 134502 (2016).
- <sup>16</sup> S.L. Bud’ko, M. Sturza, D.Y. Chung, M.G. Kanatzidis and P.C. Canfield, “Heat Capacity Jump at  $T_c$  and Pressure Derivatives of Superconducting Transition Temperature in the Ba<sub>1-x</sub>K<sub>x</sub>Fe<sub>2</sub>As<sub>2</sub> (0.2 ≤  $x$  ≤ 1.0) Series”, *Phys. Rev. B* **87**, 100509(R) (2013).
- <sup>17</sup> T. Sato, K. Nakayama, Y. Sekiba, P. Richard, Y.-M. Xu, S. Souma, T. Takahashi, G.F. Chen, J.L. Luo, N.L. Wang and H. Ding, “Band Structure and Fermi Surface of an Extremely Overdoped Iron-Based Superconductor KFe<sub>2</sub>As<sub>2</sub>”, *Phys. Rev. Lett.* **103**, 047002 (2009).

- <sup>18</sup> T.A. Maier, S. Graser, P.J. Hirschfeld, D.J. Scalapino, “D-Wave Pairing from Spin Fluctuations in the  $K_xFe_{2-y}Se_2$  Superconductors”, *Phys. Rev. B* **83**, 100515(R) (2011).
- <sup>19</sup> F. Wang, F. Yang, M. Gao, Z.-Y. Lu, T. Xiang, D.-H. Lee, “The Electron Pairing of  $K_xFe_{2-y}Se_2$ ”, *Europhys. Lett.* **93**, 57003 (2011).
- <sup>20</sup> I.I. Mazin, “Symmetry Analysis of Possible Superconducting States in  $K_xFe_ySe_2$  Superconductors”, *Phys. Rev. B* **84**, 024529 (2011).
- <sup>21</sup> P.A. Lee and X.-G. Wen, “Spin-Triplet P-Wave Pairing in a Three-Orbital Model for Iron Pnictide Superconductors”, *Phys. Rev. B* **78**, 144517 (2008).
- <sup>22</sup> D.F. Agterberg, T. Shishidou, J. O’Halloran, P.M.R. Brydon, and M. Weinert, “Resilient Nodeless D-Wave Superconductivity in Monolayer FeSe”, *Phys. Rev. Lett.* **119**, 267001 (2017).
- <sup>23</sup> P.M. Eugenio and O. Vafek, “Classification of Symmetry Derived Pairing at the M Point in FeSe”, *Phys. Rev. B* **98**, 014503 (2018).
- <sup>24</sup> M. Khodas and A.V. Chubukov, “Interpocket Pairing and Gap Symmetry in Fe-Based Superconductors with Only Electron Pockets”, *Phys. Rev. Lett.* **108**, 247003 (2012).
- <sup>25</sup> E. Berg, M.A. Metlitski and S. Sachdev, “Sign-Problem-Free Quantum Monte Carlo of the Onset of Antiferromagnetism in Metals”, *Science* **338**, 1606 (2012).
- <sup>26</sup> J.P. Rodriguez and R. Melendrez, “Fermi Surface Pockets in Electron-Doped Iron Superconductor by Lifshitz Transition”, *J. Phys. Commun.* **2**, 105011 (2018); “Corrigendum: Fermi Surface Pockets in Electron-Doped Iron Superconductor by Lifshitz Transition”, *J. Phys. Commun.* **3**, 019501 (2019).
- <sup>27</sup> C. Xu, M. Müller, and S. Sachdev, “Ising and Spin Orders in the Iron-Based Superconductors”, *Phys. Rev. B* **78**, 020501(R) (2008).
- <sup>28</sup> J. Kang and R.M. Fernandes, “Superconductivity in FeSe Thin Films Driven by the Interplay between Nematic Fluctuations and Spin-Orbit Coupling”, *Phys. Rev. Lett.* **117**, 217003 (2016).
- <sup>29</sup> J.P. Rodriguez, “Isotropic Cooper Pairs with Emergent Sign Changes in a Single-Layer Iron Superconductor”, *Phys. Rev. B* **95**, 134511 (2017).
- <sup>30</sup> S. Raghu, Xiao-Liang Qi, Chao-Xing Liu, D.J. Scalapino, Shou-Cheng Zhang, “Minimal Two-Band Model of the Superconducting Iron Oxypnictides”, *Phys. Rev. B* **77**, 220503(R) (2008).
- <sup>31</sup> J.P. Rodriguez, M.A.N. Araujo, P.D. Sacramento, “Emergent Nesting of the Fermi Surface from Local-Moment Description of Iron-Pnictide High- $T_c$  Superconductors”, *Eur. Phys. J. B* **87**, 163 (2014).

- <sup>32</sup> M. Daghofer, A. Moreo, J.A. Riera, E. Arrigoni, D.J. Scalapino, and E. Dagotto, “Model for the Magnetic Order and Pairing Channels in Fe Pnictide Superconductors”, *Phys. Rev. Lett.* **101**, 237004 (2008); A. Moreo, M. Daghofer, J.A. Riera, and E. Dagotto, “Properties of a Two-Orbital Model for Oxypnictide Superconductors: Magnetic Order,  $B_{2g}$  Spin-Singlet Pairing Channel, and its Nodal Structure”, *Phys. Rev. B* **79**, 134502 (2009).
- <sup>33</sup> P.S. Riseborough, B. Coqblin, S.G. Magalhães, “Phase Transition Arising from the Under-screened Anderson Lattice Model: A Candidate Concept for Explaining Hidden Order in URu<sub>2</sub>Si<sub>2</sub>”, *Phys. Rev. B* **85**, 165116 (2012).
- <sup>34</sup> J.P. Rodriguez, “Magnetic Excitations in Ferropnictide Materials Controlled by a Quantum Critical Point into Hidden Order”, *Phys. Rev. B* **82**, 014505 (2010).
- <sup>35</sup> P.W. Anderson, “An Approximate Quantum Theory of the Antiferromagnetic Ground State”, *Phys. Rev.* **86**, 694 (1952).
- <sup>36</sup> B.I. Halperin and P.C. Hohenberg, “Hydrodynamic Theory of Spin Waves”, *Phys. Rev.* **188**, 898 (1969).
- <sup>37</sup> D. Forster, *Hydrodynamic Fluctuations, Broken Symmetry, and Correlation Functions* (Benjamin/Cummings), Reading, MA, 1975).
- <sup>38</sup> J.P. Rodriguez, “Spin Resonances in Iron-Selenide High- $T_c$  Superconductors by Proximity to Hidden Spin Density Wave”, *Phys. Rev. B* **102**, 024521 (2020).
- <sup>39</sup> G.M. Eliashberg, “Interactions between Electrons and Lattice Vibrations in a Superconductor”, *Sov. Phys. JETP* **11**, 696 (1960).
- <sup>40</sup> G.M. Eliashberg, “Temperature Green’s Function for Electrons in a Superconductor”, *Sov. Phys. JETP* **12**, 1000 (1961).
- <sup>41</sup> J.R. Schrieffer, *Theory of Superconductivity* (Benjamin, New York, 1964).
- <sup>42</sup> D.J. Scalapino, in *Superconductivity*, v. 1, ed. R.D. Parks (Dekker, New York, 1969).
- <sup>43</sup> Y. Nambu, “Quasi-Particles and Gauge Invariance in the Theory of Superconductivity”, *Phys. Rev.* **117**, 648 (1960).
- <sup>44</sup> L.P. Gorkov, *Zh. Eksperim. i Teor. Fiz.* **34**, 735 1958; “About the Energy Spectrum of Superconductors”, *Sov. Phys. JETP* **7**, 505 (1958).
- <sup>45</sup> I.I. Mazin, D.J. Singh, M.D. Johannes, and M.H. Du, “Unconventional Superconductivity with a Sign Reversal in the Order Parameter of LaFeAsO<sub>1-x</sub>F<sub>x</sub>”, *Phys. Rev. Lett.* **101**, 057003 (2008).

- <sup>46</sup> K. Kuroki, S. Onari, R. Arita, H. Usui, Y. Tanaka, H. Kontani, and H. Aoki, “Unconventional Pairing Originating from the Disconnected Fermi Surfaces of Superconducting  $\text{LaFeAsO}_{1-x}\text{F}_x$ ”, *Phys. Rev. Lett.* **101**, 087004 (2008).
- <sup>47</sup> S. Graser, T.A. Maier, P.J. Hirschfeld, and D.J. Scalapino, “Near-Degeneracy of Several Pairing Channels in Multiorbital Models for the Fe Pnictides”, *New J. Phys.* **11**, 025016 (2009).
- <sup>48</sup> A. Linscheid, S. Maiti, Y. Wang, S. Johnston, and P.J. Hirschfeld, “High- $T_c$  via Spin Fluctuations from Incipient Bands: Application to Monolayers and Intercalates of FeSe”, *Phys. Rev. Lett.* **117**, 077003 (2016).
- <sup>49</sup> P. Morel and P.W. Anderson, “Calculation of the Superconducting State Parameters with Retarded Electron-Phonon Interaction”, *Phys. Rev.* **125**, 1263 (1962).
- <sup>50</sup> W.L. McMillan, “Transition Temperature of Strong-Coupled Superconductors”, *Phys. Rev.* **167**, 331 (1968).
- <sup>51</sup> *High-Temperature Superconductivity*, edited by V.L. Ginzburg and D.A. Kirzhnits (Consultants Bureau, New York, 1982).
- <sup>52</sup> J.P. Carbotte, “Properties of Boson-Exchange Superconductors”, *Rev. Mod. Phys.* **62**, 1027 (1990).
- <sup>53</sup> B. Pan, Y. Shen, D. Hu, Y. Feng, J.T. Park, A.D. Christianson, Q. Wang, Y. Hao, H. Wo, Z. Yin, T.A. Maier and J. Zhao, “Structure of Spin Excitations in Heavily Electron-Doped  $\text{Li}_{0.8}\text{Fe}_{0.2}\text{ODFeSe}$  Superconductors”, *Nat. Commun.* **8**,123 (2017).
- <sup>54</sup> M. Yi, Z-K Liu, Y. Zhang, R. Yu, J.-X. Zhu, J.J. Lee, R.G. Moore, F.T. Schmitt, W. Li, S.C. Riggs, J.-H. Chu, B. Lv, J. Hu, M. Hashimoto, S.-K. Mo, Z. Hussain, Z.Q. Mao, C.W. Chu, I.R. Fisher, Q. Si, Z.-X. Shen, and D.H. Lu, “Observation of Universal Strong Orbital-Dependent Correlation Effects in Iron Chalcogenides”, *Nat. Comm.* **6**, 7777 (2015).
- <sup>55</sup> R. Yu and Q. Si, “Orbital-Selective Mott Phase in Multiorbital Models for Alkaline Iron Selenides  $\text{K}_{1-x}\text{Fe}_{2-y}\text{Se}_2$ ”, *Phys. Rev. Lett.* **110**, 146402 (2013).
- <sup>56</sup> See Supplemental Material: I. Add  $3d_{xy}$  Orbital to Eliashberg Theory with  $3d_{xz}/3d_{yz}$  Orbitals; II. Effects and Properties of  $3d_{xy}$  Orbital; III. Spin-Orbit Coupling.
- <sup>57</sup> O.V. Dolgov, I.I. Mazin, D. Parker, A.A. Golubov, “Interband Superconductivity: Contrasts between BCS and Eliashberg Theory”, *Phys. Rev.* **B79**, 060502(R) (2009); O.V. Dolgov, I.I. Mazin, D. Parker, A.A. Golubov, “Erratum: Interband Superconductivity: Contrasts between Bardeen-Cooper-Schrieffer and Eliashberg Theories [Phys. Rev. B 79, 060502(R) (2009)]”, *Phys.*



Rev. B **80**, 219901(E) (2009).

- <sup>58</sup> L. Benfatto, E. Cappelluti, and C. Castellani, “Spectroscopic and Thermodynamic Properties in a Four-Band Model for Pnictides”, Phys. Rev. B **80**, 214522 (2009).
- <sup>59</sup> G. A. Ummarino, M. Tortello, D. Daghero, and R. S. Gonnelli “Three-Band  $s\pm$  Eliashberg Theory and the Superconducting Gaps of Iron Pnictides” Phys. Rev. B **80**, 172503 (2009).